A quantitative ultrastructural timeline of nuclear autophagy reveals a role for dynamin-like protein 1 at the nuclear envelope

Philip J. Mannino[1], Andrew Perun[1], Ivan Surovstev[1,2], Nicholas R. Ader[1], Lin Shao[1], Thomas J. Melia[1], Megan C. King[1,3], and C. Patrick Lusk[1&]

[1]Department of Cell Biology, Yale School of Medicine, 295 Congress Ave, New Haven, CT, 06520

[2]Department of Physics, Yale University, New Haven, CT, 06511

[3]Department of Molecular Cellular and Developmental Biology, Yale University, New Haven, CT, 06511

[&]Correspondence to C. Patrick Lusk

patrick.lusk@yale.edu

Abstract

Autophagic mechanisms that maintain nuclear envelope homeostasis are bulwarks to aging and disease. By leveraging 4D lattice light sheet microscopy and correlative light and electron tomography, we define a quantitative and ultrastructural timeline of a nuclear macroautophagy (nucleophagy) pathway in yeast. Nucleophagy initiates with a rapid local accumulation of the nuclear cargo adaptor Atg39 at the nuclear envelope adjacent to the nucleus-vacuole junction and is delivered to the vacuole in ~300 seconds through an autophagosome intermediate. Mechanistically, nucleophagy incorporates two consecutive and genetically defined membrane fission steps: inner nuclear membrane (INM) fission generates a lumenal vesicle in the perinuclear space followed by outer nuclear membrane (ONM) fission to liberate a double membraned vesicle to the cytosol. ONM fission occurs independently of phagophore engagement and instead relies surprisingly on dynamin-like protein1 (Dnm1), which is recruited to sites of Atg39 accumulation at the nuclear envelope. Loss of Dnm1 compromises nucleophagic flux by stalling nucleophagy after INM fission. Our findings reveal how nuclear and INM cargo are removed from an intact nucleus without compromising its integrity, achieved in part by a non-canonical role for Dnm1 in nuclear envelope remodeling.

Introduction

The nuclear envelope (NE) establishes the boundary between cytoplasm and nucleoplasm. Although it shares a contiguous lumen with the endoplasmic reticulum (ER), it is functionally specialized by the unique proteomes and lipidomes that distinguish at least three membranes: the inner nuclear membrane (INM) that engages with the genome and in some eukaryotes, a nuclear lamina, an outer nuclear membrane (ONM) that connects with the cytoskeleton, and a pore membrane that houses nuclear pore complexes (NPCs). As for all organelles, NE proteins are subject to proteostasis mechanisms that include the ubiquitin-proteasome and autophagy pathways[1]. These degradative processes are triggered upon molecular damage or genetic perturbation to NE components[2-4], nutrient deprivation[5], mislocalization of integral membrane proteins to the INM[6-8], senescence[9], during the meiotic program[10,11], and in the context of other cellular stresses[12]. Although turnover of the NE is important to maintain cellular homeostasis by combatting the accumulation of deleterious factors associated with disease and aging[13], the underlying mechanisms remain to be fully defined.

Of the two major protein degradation pathways, autophagy recycles a broader spectrum of molecules including protein aggregates, nucleic acids, and lipids. The latter may be particularly important at the nucleus as the NE is sensitive to perturbations in lipid composition[14-17] and metabolism[18-20]. Autophagy delivers molecules (“cargo”) for degradation in lysosomes (in metazoans) or vacuoles (in yeast and plants) either directly through microautophagy or indirectly through macroautophagy, which incorporates a double membrane autophagosome intermediate[21]. The precursor to the autophagosome, the phagophore or isolation membrane, is a cup shaped double

membrane that forms de novo and expands around cargo. There are both non-selective and selective macroautophagy pathways with the latter defined by cargo adaptor proteins that recruit the phagophore to specific cellular sites by directly engaging membrane-associated proteins on the phagophore, most commonly lipidated LC3 (Atg8 in yeast)[21].

Both micro and macroautophagy pathways act on the nucleus. For example, mammalian cells execute a form of nuclear microautophagy whereby the ONM selectively buds into lysosomes[22]. Similarly, piecemeal microautophagy of the nucleus (PMN) in yeast involves the coordinated evagination of both the INM and ONM directly into the vacuole[23]. The forms of nuclear macroautophagy described to date are comparatively less well understood and atypical as selectivity is imparted by direct interactions between Atg8/LC3 and the cargo instead of through a dedicated cargo adaptor. These pathways include the clearance of Lamin B1 under conditions of oncogene-induced senescence[9] and NPCs by “NPC-phagy”[24-26]. In contrast, recent work in budding yeast identified the first nuclear-specific cargo adaptor, Atg39[27], that is required for the degradation of both soluble nuclear and integral membrane cargo[27-29]. However, in this pathway, and indeed all forms of nuclear autophagy, the NE remodeling mechanisms required to selectively remove components of the nucleus, INM, and ONM remain mechanistically opaque.

Because Atg39 is a cargo adaptor and is consumed by autophagy[27], it provides an ideal molecular handle to investigate the kinetics and NE remodeling steps of a model nuclear macroautophagy (hereafter called nucleophagy) pathway. Atg39 is a single pass integral ONM protein[30,31] with Atg8 and Atg11 (an autophagy scaffold protein) interacting

87 motifs on its cytosolic N-terminus[27]. The C-terminal lumenal domain has several
88 amphipathic helices that engage the lumenal leaflet of the INM[30,31]. Thus, Atg39 forms a
89 translumenal bridge that physically couples the INM and ONM and likely coordinates
90 their remodeling during nucleophagy. Consistent with this, the Atg39 lumenal
91 amphipathic helices are required for nucleophagic degradation of nuclear and INM
92 cargos[30,31]. Further, Atg39 overexpression drives elaborate NE blebbing where both
93 membranes of the NE are evaginated[30,31]. However, as these NE blebs remain
94 associated with the NE in the absence of autophagy induction, there remains
95 uncertainty as to the precise membrane remodeling events orchestrated by Atg39 in the
96 physiological state, which must be understood at the ultrastructural and molecular
97 levels.

98 Two hypothetical models have been proposed for Atg39-mediated nucleophagy[1]. In
99 the first model, two sequential membrane fission events are invoked, first at the INM to
100 generate an INM-derived vesicle (INMDV) in the perinuclear space/NE lumen and the
101 second at the ONM to release a nucleus-derived vesicle (NDV) (Figure S1A). In the
102 second model, the INM and ONM are simultaneously evaginated and an NDV is
103 liberated from the NE through coincident ONM and INM fission events (Figure S1B).
104 Here, we use a combination of lattice light sheet microscopy (LLSM) and correlative
105 light and electron microscopy (CLEM) and tomography to describe the kinetic and
106 ultrastructural steps of nucleophagy. Our data firmly establish that nucleophagy
107 proceeds through an INMDV intermediate followed by an ONM fission step that requires
108 Dnm1, a dynamin-like protein that was formerly established to function only in

109 mitochondrial[32] and peroxisomal[33] fission. Thus, we significantly advance a molecular
110 and morphological understanding of nucleophagy.

111 **Results**

112 **Dnm1 is required for robust nucleophagic flux**

113 To identify membrane remodeling factors that contribute to nucleophagy, we
114 assessed the autophagic flux of Atg39 by modeling an approach used to monitor ER-
115 phagy[34]. We generated yeast strains producing an Atg39 fusion protein with a variation
116 of the Rosella[35] biosensor that is comprised of a tandem pH-sensitive GFP
117 (pHluorin/pHn) and pH-insensitive mCherry/mCh (Figure 1A,B). Atg39-pHn-mCh was
118 expressed from the *ATG39* chromosomal locus with the endogenous 3'UTR intact. We
119 determined that preserving the *ATG39* 3'UTR was essential for optimal expression of
120 Atg39 fusion proteins, particularly when stimulated under conditions of nitrogen
121 starvation but not Tor1-inhibition using rapamycin (Figure S1C-E).

122 After culturing cells without nitrogen, both red-only and red-green Atg39-pHn-mCh
123 fluorescent foci are observed in wildtype (WT) cells (Figure 1B,C). We calculated a
124 nucleophagic flux value as a ratio of the number of red fluorescent-only foci (i.e. those
125 delivered to the vacuole where the pHn fluorescence is quenched) to the total number
126 of foci in a cell; this ratio was then normalized to 1 for WT cells. We then related this
127 value to Atg39-pHn-mCh fluxes calculated from a battery of candidate yeast deletion
128 strains lacking genes that contribute to macroautophagy (*ATG8*, *ATG11*)[36,37], PMN
129 (*NVJ1*)[38], NE homeostasis (*HEH1*, *HEH2*, *CHM7*)[39-42], ER-phagy (*VPS13, LST1, SCS2,*
130 *LNP1*)[43-46], ER shaping/remodeling (*SEY1, RTN1, RTN2, YOP1*)[47,48], mitochondrial

Figure 1

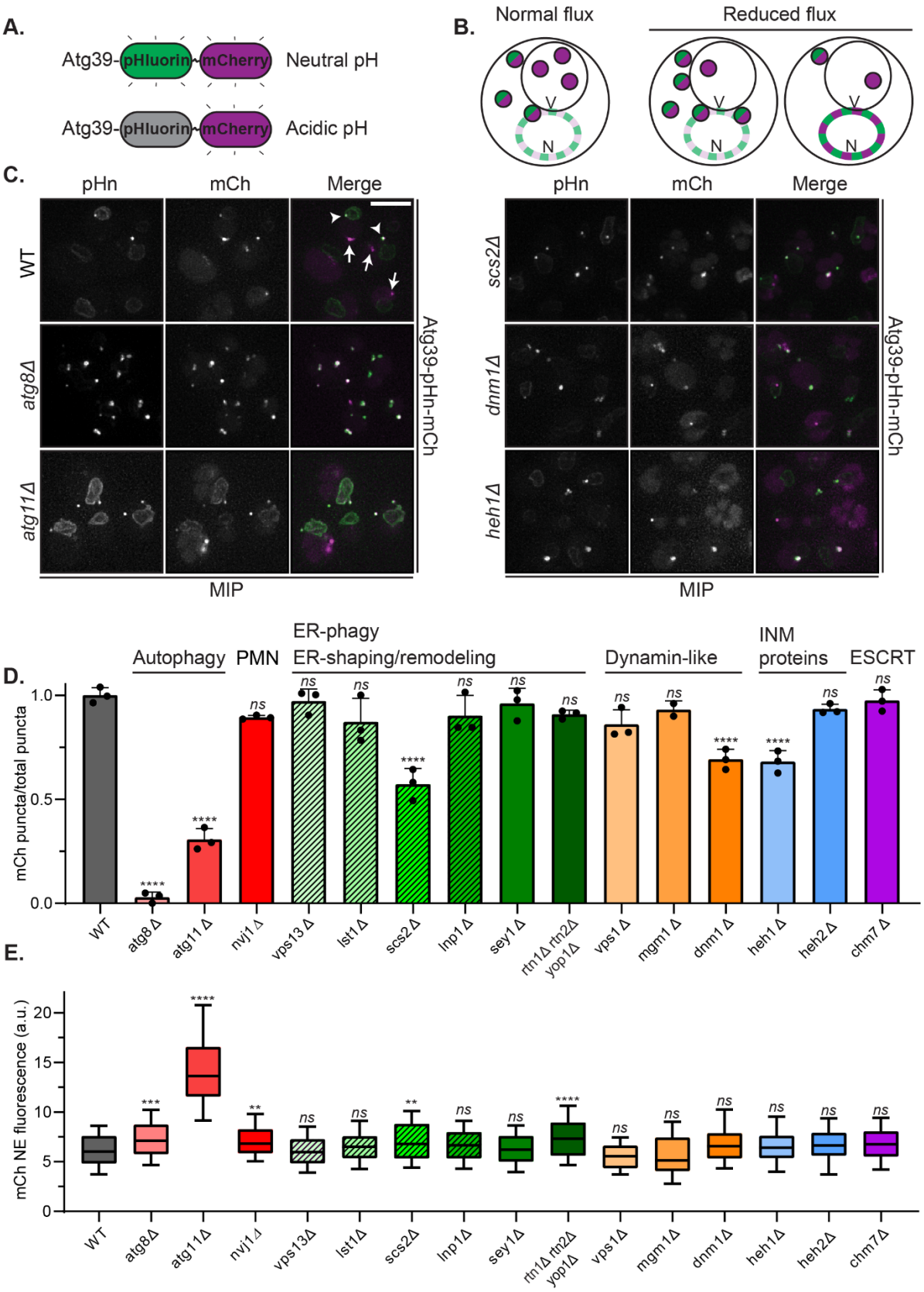
A.
Atg39-pHluorin-mCherry
Neutral pH
Atg39-pHluorin-mCherry
Acidic pH
B.
Normal flux
Reduced flux
V
N
C.
pHn
mCh
Merge
WT
atg8Δ
atg11Δ
scs2Δ
dnm1Δ
heh1Δ
Atg39-pHn-mCh
MIP
D.
Autophagy
PMN
ER-phagy
ER-shaping/remodeling
Dynamin-like
INM proteins
ESCRT
mCh puncta/total puncta
1.0
0.5
0.0
ns
****
WT
atg8 Δ
atg11 Δ
nvj1 Δ
vps13 Δ
lst1 Δ
scs2 Δ
lnp1 Δ
sey1 Δ
rtn1Δ rtn2Δ yop1Δ
vps1 Δ
mgm1 Δ
dnm1 Δ
heh1 Δ
heh2 Δ
chm7 Δ
E.
mCh NE fluorescence (a.u.)
20
15
10
5
0
***
**
****
ns
WT
atg8Δ
atg11Δ
nvj1Δ
vps13Δ
lst1Δ
scs2Δ
lnp1Δ
sey1Δ
rtn1Δ rtn2Δ yop1Δ
vps1Δ
mgm1Δ
dnm1Δ
heh1Δ
heh2Δ
chm7Δ

131

Figure 1 – Dnm1 is required for nucleophagic flux of an Atg39 reporter.

A) Schematic of Atg39-pHn-mCh construct that has red and green fluorescence in neutral pH and only red fluorescence (magenta) in acidic environments like the vacuole.

B) Potential outcomes and interpretation of Atg39-pHn-mCh flux experiment. Schematic of cells (N, nucleus; V, vacuole) with Atg39-pHn-mCh foci diagrammed as either green/red or red; reduced flux can also manifest as an increase in Atg39-pHn-mCh fluorescence at the NE (far right).

C) Fluorescence micrographs of cells expressing Atg39-pHn-mCh in the indicated genetic backgrounds after 6 h in medium lacking nitrogen. Green (pHn), red (mCh) channels and merge shown. In all panels a maximum intensity projection (MIP) of a deconvolved z-series of images of entire cell volumes are shown. Arrowheads indicate green/red foci; arrows denote red only foci. Scale bar is 5 µm.

D) Bar graph of the mean ratios of mCherry-only fluorescent Atg39-pHn-mCh foci to the total number of foci in individual cells of indicated genotypes relative to this ratio in WT cells. Error bars are standard deviation from the mean of three biological replicates (black dots). Genotype labels are organized by established function (described above the graph) of the proteins they are missing. Dashed lines on the green bar graphs indicate genes required for ER-phagy. Ordinary one-way ANOVA with multiple comparisons, n=300 cells, at least 100 cells per biological replicate. ****P<0.0001; *ns*, not significant.

E) Box plot of the mean mCherry fluorescence intensity at the nuclear envelope at regions devoid of foci. Error bars indicate the standard deviation of the mean between three biological replicates. Ordinary one-way ANOVA with multiple comparisons, n=300 cells, at least 100 cells per biological replicate. ****P<0.0001; ***P<0.001; **P<0.01; *ns*, not significant.

132 fission and fusion (*DNM1, MGM1*)[49,50] and endocytosis (*VPS1*)[51]. Consistent with the
133 conclusion that this approach reported on perturbations to nucleophagy, Atg39-pHn-
134 mCh flux was nearly abolished in *atg8Δ* cells and severely attenuated in the absence of
135 *ATG11* (Figure 1C,D). In the latter case, we also observed an increase of Atg39-pHn-
136 mCh fluorescence throughout the entire nuclear periphery, suggesting that Atg11 may
137 contribute to early nucleophagy events required for Atg39's focal accumulation at the
138 NE (Figure 1C,E). Thus, this assay also provides insight into the step at which a given
139 factor may impact nucleophagy.

140 We did not observe any major impact on Atg39-pHn-mCh flux or NE accumulation
141 after perturbing PMN by deletion of *NVJ1*. Likewise, most tested membrane remodeling
142 deletion strains had normal nucleophagic flux, although we note that there were modest
143 increases in NE fluorescence that met reasonable statistical significance in the context
144 of the *rtn1Δrtn2Δyop1Δ* strain, which has perturbed ER morphology[48]. In marked
145 contrast, we observed a robust 30-45% reduction in the delivery of Atg39-pHn-mCh to

146 the vacuole in *scs2Δ*, *dnm1Δ*, and *heh1Δ* strains (Figure 1C,D). Of these, Dnm1
147 (orthologue of DRP1) stood out as it is part of the dynamin family of GTPases with well-
148 established roles in driving membrane fission[52]. While it is known that Dnm1 functions at
149 mitochondria and peroxisomes, there is no evidence that it acts at the NE.

150 **Dnm1 colocalizes with Atg39 during nucleophagy**

151 In a model where Dnm1 functions during nucleophagy, it is expected to engage
152 Atg39. We therefore tested colocalization between endogenously expressed Dnm1-
153 mCherry and Atg39-GFP during LLSM timelapse imaging (10 second intervals) of live
154 cells under nitrogen starvation. To avoid recording spurious colocalization events
155 between the abundant mitochondrial/peroxisomal-localized Dnm1[32] and Atg39, we
156 performed this analysis in the absence of Fis1, which is required to recruit Dnm1 to
157 mitochondria[49] and peroxisomes[53]. To assess colocalization in an unbiased manner, we
158 used custom MATLAB scripts to identify Atg39-GFP and Dnm1-mCherry fluorescent foci
159 and measure the distance between Atg39-GFP and the most proximal Dnm1-mCherry
160 spot (Figure S2A,B). We considered Atg39-GFP and Dnm1-mCherry foci colocalized
161 when the centers of their signals were within 400 nm as at this distance signal overlap
162 was empirically observed. We also recorded the timing of colocalization relative to the
163 onset of nucleophagy defined as the first observation of an Atg39-GFP focus in a cell.
164 Using these criteria, we detected colocalization in 65% of Atg39-GFP trajectories (*n*=43;
165 Figure 2C; yellow). Individual colocalization events typically persisted for only one frame
166 (i.e. less than 20 seconds) and occurred from 70 to 490 seconds after Atg39-GFP focus
167 formation (median of 170 seconds; Figure 2D; yellow). Colocalization events that
168 persisted for 2-3 frames (10-40 seconds) were less frequent (11 out of 43) with a

169 median of 160 seconds (Figure 2D; green). Consistent with the notion that Dnm1 was

Figure 2

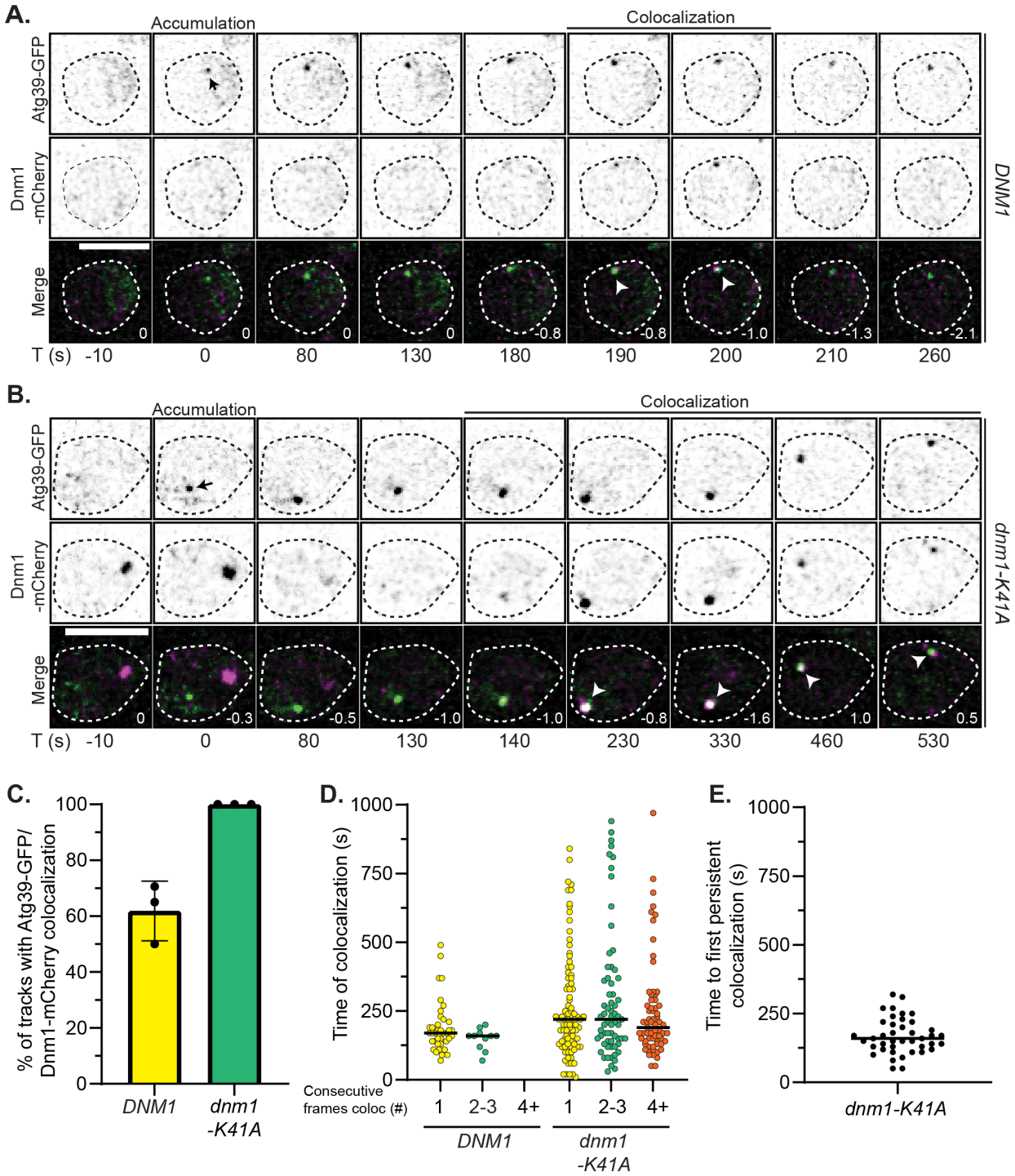

Figure 2 – Dnm1 is recruited to Atg39 during nucleophagy

A, B) Inverted fluorescent micrographs of a timelapse series (10 s intervals) of *fis1Δ* cells expressing Atg39-GFP and Dnm1-mCherry with either an extra copy of *DNM1* or the dominant negative *dnm1-K141A* allele under conditions of nitrogen starvation. Green and red channels shown with merge at indicated times (T) with T=0 s being the first detection of a Atg39-GFP focus (arrow). Arrowheads point to colocalization between Atg39-GFP and Dnm1-mCherry. Numbers in merge are the z-position (in μm) of the image shown in reference to the midplane. Scale bars are 5 μm.

C) Plot of the percentage of Atg39-GFP foci that were continuously tracked from their point of origin by timelapse microscopy that colocalize with Dnm1-mCherry at least once during the timelapse image series. For cells expressing *DNM1* *n*=43 cells, 43 tracks, 3 biological replicates. For cells expressing *dnm1-K41A* *n*=59 cells, 59 tracks, 3 biological replicates. Mean and standard deviation from three biological replicates (black dots).

D) A scatter plot of the time between the appearance of an Atg39-GFP focus and colocalization of Atg39-GFP and Dnm1-mCherry. Data are binned by the number of consecutive frames (10 s intervals) colocalization was observed in *fis1Δ* cells expressing *DNM1* or *dnm1-K141A*. The black bar is the median.

E) As in D but only plotting the time to the first Atg39-GFP Dnm1-mCherry colocalization that persisted for 4 or more frames in cells expressing *dnm1-K41A*.

170 acting on Atg39-containing structures, we observed that the dynamics of Atg39-GFP
171 increased following its colocalization with Dnm1-mCherry as assessed by an elevation
172 of its mean displacement (Figure S2C) after the colocalization events.

173 As most Atg39-Dnm1 colocalization events were short lived, we tested if we could
174 stabilize their association by expressing a dominant-negative *dnm1-K41A* allele[54] that
175 produces a GTPase-dead form of Dnm1 that binds, but does not hydrolyze GTP[54]. At
176 mitochondria, this dominant negative protein traps endogenous Dnm1 as a membrane-
177 bound oligomer and thus prevents membrane fission[54]. Strikingly, we observed
178 colocalization between Dnm1-mCherry and Atg39-GFP in all *dnm1-K41A* expressing
179 cells (*n*=59; Figure 2C; green) that often persisted beyond 40 seconds and indeed could
180 last throughout our observation window (>350 seconds; Figure 2D, S2B). These
181 colocalizations persisted even as the pair of foci moved together (Figure 2B), strongly
182 suggesting that they associated with the same structure. Interestingly, the median time
183 of the first colocalization event that persisted for 4 frames or more (more than 30
184 seconds) was 160 seconds (Figure 2E). Thus, when taken together, the data support

185 that Dnm1 is recruited to sites of Atg39-accumulation after ~3 minutes. Consistent with
186 studies demonstrating that Atg11 directly recruits Dnm1 in the context of mitophagy[55]
187 and pexophagy[56], we also observed that Atg11 was required for the recruitment of
188 Dnm1 to the NE (Figure S2D,E).

189 **Quantitative analysis of Atg39 dynamics**

190 To better interpret the timing of Dnm1 recruitment to Atg39, we needed a clear
191 accounting of the molecular, kinetic, and morphological steps that comprise
192 nucleophagy. We therefore performed LLSM timelapse imaging of Atg39-GFP under
193 conditions of nitrogen starvation in WT cells. To facilitate monitoring the delivery of
194 Atg39-GFP into vacuoles, we performed these experiments in cells expressing Vph1-
195 mCherry to visualize vacuolar membranes. We measured the intensity of Atg39-GFP
196 foci and used commercial (Imaris) and our own particle tracking algorithms[57-59] to
197 quantitatively evaluate their initial appearance at the NE, their rate of growth, and their
198 delivery to the vacuole – all of which occurred at a rate of 1.4 events/cell/hour (Movie 1).

199 Atg39-GFP was first visible diffusely localized along the nuclear rim before it
200 concentrated into a single focus (Figure 3A). Of note, Atg39 always (*n*=221/221)
201 accumulated directly adjacent to the nucleus-vacuole junction (NVJ), suggesting that
202 nucleophagy may occur at a privileged domain on the NE and/or vacuole (Figure 3A).
203 At this site, Atg39-GFP fluorescence rapidly increased by over 4-fold and then leveled
204 off by ~100 seconds before a slow diminishment that likely reflected photobleaching
205 (Figure 3C; blue, circles). A molecular counting strategy based on relating the
206 fluorescence of Atg39-GFP foci to a GFP standard of known copy number (Fta3-
207 GFP[60])(Figure S1F) indicated that the mean number of Atg39-GFP molecules in a

208 given focus at steady state was ~190 (Figure 3D; blue). We estimate, based on the

Figure 3

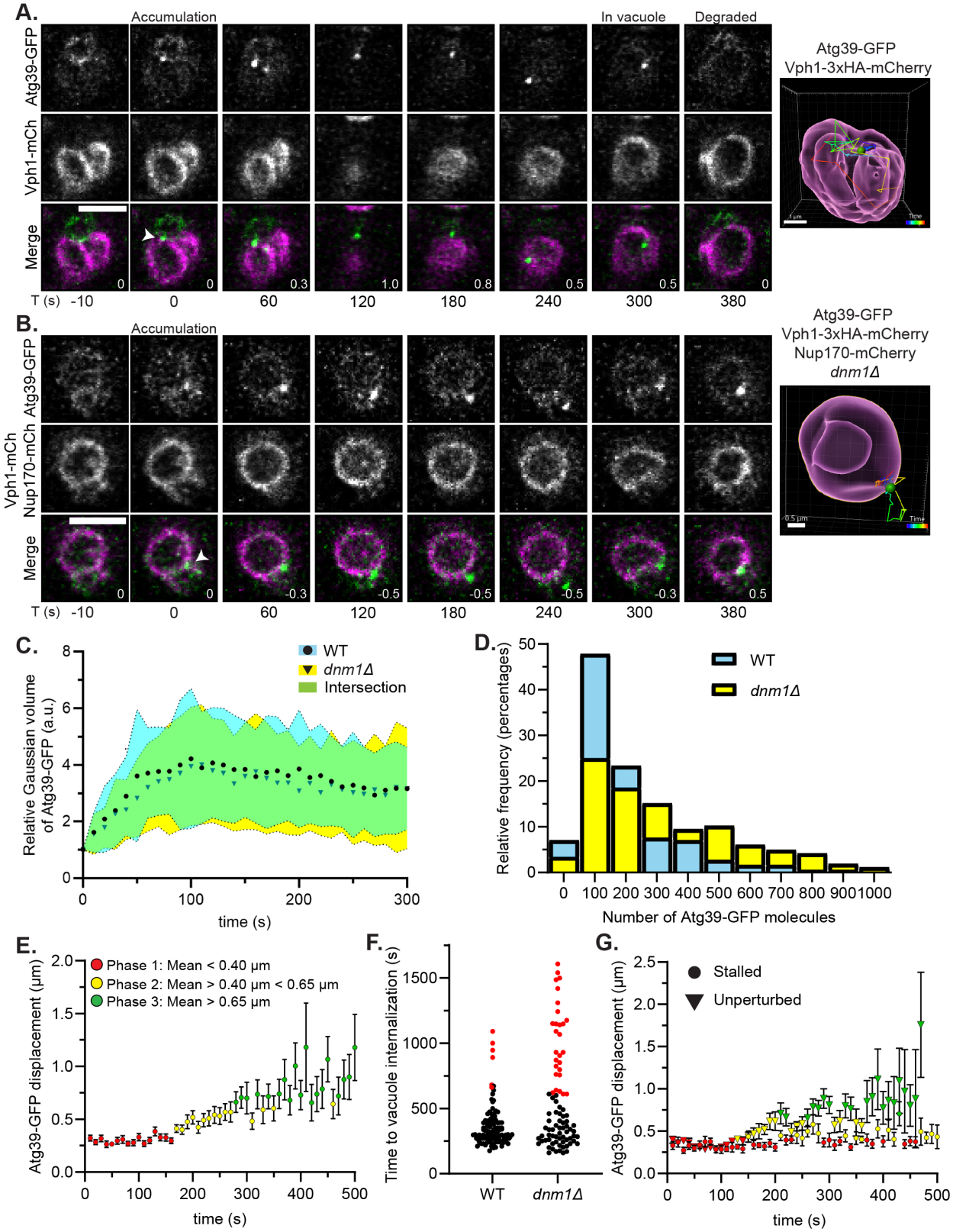

Figure 3 – Dnm1 impacts Atg39 dynamics, copy number, and robust delivery to vacuole.

A) Fluorescent micrographs from a timelapse series of WT cells expressing Atg39-GFP and Vph1-mCherry (mCh) imaged every 10 seconds in medium lacking nitrogen. Green, red (magenta) and merge shown. Images shown from 10 s before focal accumulation (arrowhead; T=0) and every 60 s after until Atg39-GFP fluorescence disappears in the vacuole (Degraded). Numbers in merge are the z-position (in μm) of the image shown in reference to the midplane. Scale bar is 3 μm. The panel at right shows a 3D model with particle track of Atg39-GFP focus color coded by time. Vph1-mCherry was rendered as a magenta surface and Atg39-GFP as a green ball. The length of the scale bar is indicated in the image on the right.

B) As in A but *dnm1Δ*.

C) Fluorescence intensity of Atg39-GFP foci plotted versus time after their first detection. Shaded areas are the standard deviation.

D) Histogram of the distribution of the number of Atg39-GFP molecules per focus at steady state in cells of the indicated genotypes cultured for 4 h without nitrogen.

E) Plot of the mean displacement and SEM of Atg39-GFP foci over time in WT cells. The points are colored as indicated in the legend. *n*=40 cells from three biological replicates.

F) Scatter plot of the time between the initial identification of an Atg39-GFP focus in WT and *dnm1Δ* cells and the internalization into the vacuole. Red dots indicate instances in which the Atg39-GFP particle never entered the vacuole after at least ten minutes.

G) As in **E** but *dnm1Δ* cells. Atg39-GFP tracks were grouped together based on whether they were internalized (unperturbed) or not (stalled) in vacuoles. *n*=37 unperturbed tracks and *n*=19 stalled tracks.

lowest 10% of Atg39-GFP molecules in a given focus, that early NE accumulations of Atg39-GFP contain roughly ~30-50 molecules. These data indicated that ~50-100 molecules were added per minute during the initial phase (Figure 3C,D). By decreasing the time step from 10 seconds to 2 seconds, we observed that the increase in Atg39-GFP focal intensity likely occurs by the coalescence with smaller NE foci (Figure S3A).

To quantitatively describe Atg39's journey from the NE to the vacuole, we measured the 10 second displacements of each of 40 Atg39-GFP foci over 20-minute timelapse experiments from the first frame of their NE focal accumulation. A consistent theme emerged in which the Atg39-GFP tracks could be empirically categorized into three bins based on characteristic mean displacements for each time point (Figure 3E). In an initial phase that extended until ~160 seconds, Atg39-GFP foci were constrained with average displacements of 0.30 ± 0.03 μm (Figure 3E; red). This was followed by ~100 seconds where the average displacement roughly doubled to 0.52 ± 0.08 μm

222 (Figure 3E; yellow). Finally, at ~280 seconds Atg39-GFP foci entered a highly mobile
223 state with a mean displacement of 0.82 ± 0.18 μm (Figure 3E; green). Thus, Atg39-
224 GFP foci transition from a constrained to a highly mobile state during nucleophagy.

225 The categorization of Atg39-GFP dynamics into three states provided a useful
226 framework to interpret and temporally align key molecular events. For example, manual
227 inspection of all Atg39-GFP tracks with the vacuolar membrane marker (Vph1-
228 mCherry) indicated that delivery into the vacuole lumen occurred within a range of 3 to
229 8 minutes after Atg39-GFP accumulation with a median of ~284 seconds (Figure 3A,F;
230 black dots), strikingly like the timing of the transition from phase 2 to 3. Likewise, the
231 transition from phase 1 to 2 occurs with timing that corresponds to the median timing of
232 Dnm1 recruitment (i.e. ~160 seconds after Atg39-GFP accumulation, Figure 2D,E).
233 Further, and consistent with the interpretation that phase 1 reflects the dynamics of
234 Atg39 at the NE, we observed that a model INM cargo colocalizes with Atg39-GFP foci
235 with a mean timing of ~80 seconds after Atg39-GFP accumulation (Figure S3D,E).
236 Thus, together these data predict that Dnm1 contributes to a key transition step in
237 nucleophagy that corresponds to a step after cargo delivery and between the NE and
238 vacuole.

239 **Nucleophagy stalls in the absence of Dnm1**

240 To explore a model in which Dnm1 acts at a transition between phase 1 and 2, we
241 monitored Atg39-GFP dynamics in *dnm1Δ* cells. Interestingly, early events including the
242 formation of the Atg39-GFP foci proximal to the NVJ (Figure 3B) and the initial rate of
243 Atg39-GFP accumulation (Figure 3C; yellow, triangles) were indistinguishable between
244 WT and *dnm1Δ* cells. However, analyzing Atg39-GFP copy number within individual foci

245 at steady state revealed an increase to a mean of 335 molecules in *dnm1Δ* cells
246 compared to 190 in WT cells (Figure 3D; yellow). Taken together, these data suggest
247 that *dnm1Δ* cells contain a population of Atg39-GFP foci that accumulate additional
248 molecules in a timeframe beyond 300 seconds, implying their delivery to the vacuole
249 may be impaired.

250 Our prior observations suggested only a partial compromise in nucleophagic flux in
251 the absence of *DNM1* (Figure 1D), and indeed, in the instances where Atg39-GFP was
252 delivered to the vacuole in *dnm1Δ* cells, it did so with timing comparable to WT cells
253 (Figure 3F; black dots). However, ~32% of Atg39-GFP foci that were tracked from their
254 NE accumulation forward failed to enter the vacuole over the experimental timeframe
255 compared to only ~5% in WT cells (Figure 3F; red dots, Figure S3B). Thus, consistent
256 with the initial nucleophagic flux assay, these observations suggest that Dnm1 is
257 required for the delivery of at least a third of Atg39 to the vacuole. We next assessed
258 the dynamics of Atg39-GFP foci in *dnm1Δ* cells. As our data suggested at least two
259 fates of Atg39 in *dnm1Δ* cells, we measured the displacement of the "stalled" (Dnm1-
260 dependent; Figure 3G; circles) and "unperturbed" (Dnm1-independent; Figure 3G;
261 triangles) Atg39-GFP tracks separately and color-coded the data using the three states
262 defined in Figure 3E. Strikingly, whereas the unperturbed tracks exhibited dynamics that
263 were similar to WT cells, the stalled tracks had mean displacements that mirror those in
264 the first phase, consistent with the notion that the transition from phase 1 to phase 2
265 was disrupted by loss of *DNM1* in these cells (Figure 3G). Indeed, the relative time that
266 the stalled Atg39 tracks spent in phase 1 doubled compared to both WT cells and the
267 unperturbed tracks in *dnm1Δ* cells (Figure S3C). Thus, these data support a model in

268 which Dnm1 is required to release Atg39 from the confines of the NE in at least a third
269 of all nucleophagy events.

270 **Nucleophagy proceeds through a lumenal vesicle intermediate**

271 We next sought to correlate Atg39's dynamics in WT and *dnm1Δ* cells to an
272 ultrastructural description of nucleophagy by CLEM and tomography. This analysis was
273 enabled by the recently developed hyper folder YFP (hfYFP), which retains significantly
274 more fluorescence compared to mEGFP following fixation, staining, and embedding[61].
275 As we lack an approach to synchronize nucleophagy, we acquired tomograms from
276 randomly selected Atg39-hfYFP foci, avoiding those that were within the vacuole lumen.
277 As CLEM is laborious and low-throughput, we used probability theory to establish a
278 target of ~30 tomograms, which would allow us to capture at least one image
279 representative of all morphological steps that last longer than 30 seconds given that it
280 takes ~300 seconds to complete nucleophagy. Thus, morphologies comprising phase 1
281 (160 seconds) and 2 (100 seconds) should be highly represented and perhaps those
282 invisible to the quantitative light microscopy analysis could also be revealed.

283 We obtained 32 tomograms in WT cells where we correlated the fluorescence of
284 Atg39-hfYFP to the underlying ultrastructure (Figure 4A-E; Figure S4A-E). We observed
285 several morphologies that are illustrated with categorization labels (1-4) in Figure 4F;
286 the number of tomograms representative of each morphology is plotted in Figure 4G
287 (blue bars). We made several observations: 1) Approximately half (15/32) of the Atg39-
288 hfYFP foci correlated to regions of NE (Figure 4A) or, surprisingly, ER (Figure 4B; Figure
289 S4A-C), with intralumenal vesicles that we interpret as INMDVs; in the latter we often
290 visualized a nearby ER-NE junction within the 3D volume of the tomogram (e.g. Figure

Figure 4

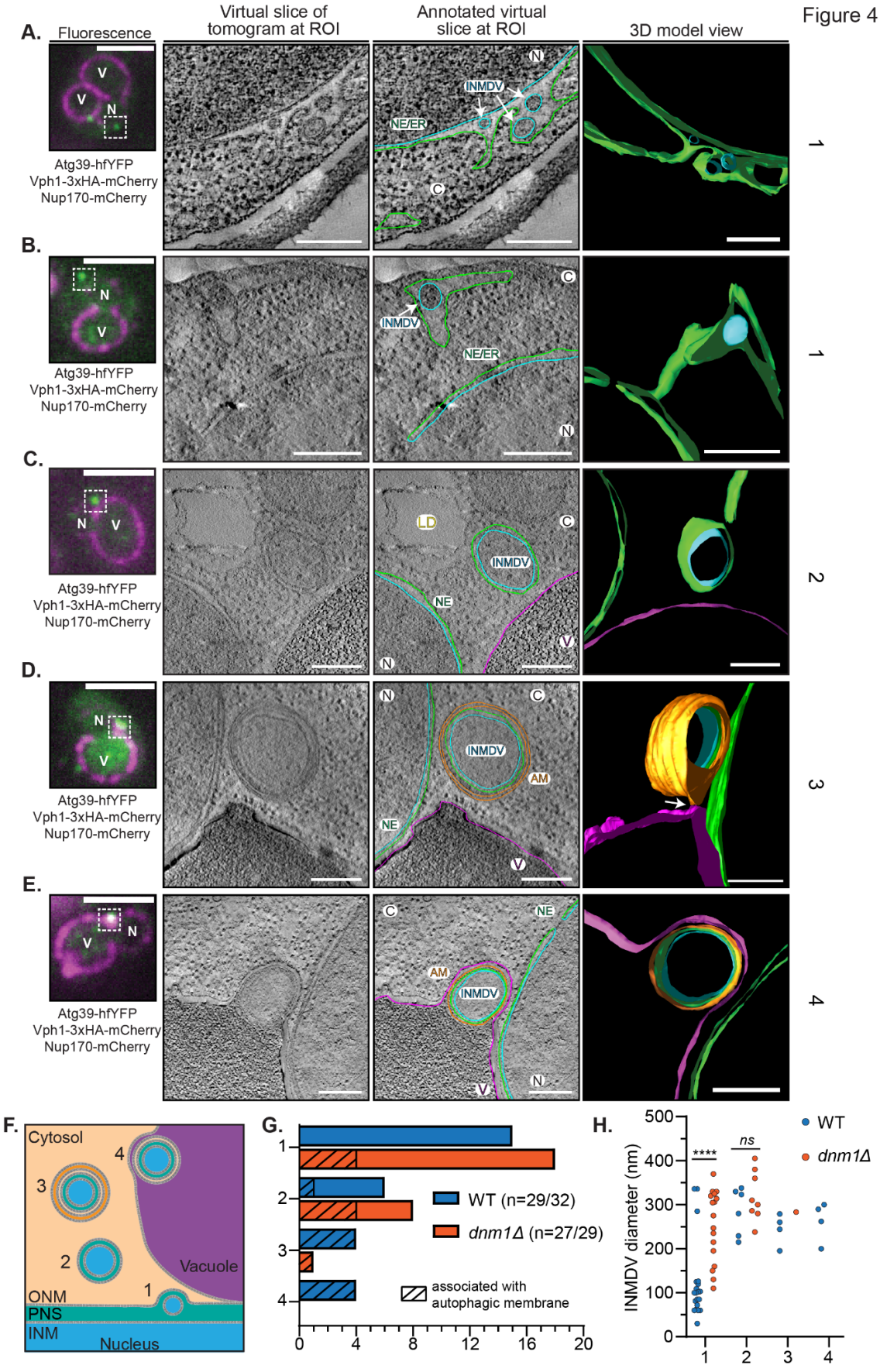
A.
Fluorescence
Virtual slice of tomogram at ROI
Annotated virtual slice at ROI
3D model view
V
V
N
Atg39-hfYFP
Vph1-3xHA-mCherry
Nup170-mCherry
N
INMDV
NE/ER
C
1
B.
N
V
Atg39-hfYFP
Vph1-3xHA-mCherry
Nup170-mCherry
C
INMDV
NE/ER
N
1
C.
N
V
Atg39-hfYFP
Vph1-3xHA-mCherry
Nup170-mCherry
LD
C
INMDV
NE
V
N
2
D.
N
V
Atg39-hfYFP
Vph1-3xHA-mCherry
Nup170-mCherry
N
C
INMDV
AM
NE
V
3
E.
V
N
Atg39-hfYFP
Vph1-3xHA-mCherry
Nup170-mCherry
C
NE
AM
INMDV
V
N
4
F.
Cytosol
4
3
2
1
Vacuole
ONM
PNS
INM
Nucleus
G.
1
2
3
4
WT (n=29/32)
dnm1Δ (n=27/29)
associated with autophagic membrane
0
4
8
12
16
20
H.
500
400
300
200
100
0
INMDV diameter (nm)
****
ns
WT
dnm1Δ
1
2
3
4

291

Figure 4 – Nucleophagy proceeds through a lumenal vesicle intermediate.

A-E) CLEM/tomography of sites of Atg39-hfYFP foci. From left to right: fluorescence image of WT cells expressing Atg39-hfYFP (green), Vph1-mCherry and Nup170-mCherry (magenta). Scale bar is 3 µm. EM tomogram acquired of boxed region in fluorescence image and tomogram virtual slice without and with annotation shown alongside a snapshot of a 3D model. Arrows point to INMDVs. ONM is green, INM is light blue, phagophore/autophagosome is orange, vacuole membrane is magenta. Scale bar is 200 nm. C, cytosol; N, nucleus; V, vacuole; NE, nuclear envelope; ER, endoplasmic reticulum; INMDV, inner nuclear membrane derived vesicle; AM, autophagic membrane; LD, lipid droplet. Numbers at right refer to classification scheme in **F**. Arrow indicates a site of close apposition between the outer membrane of the autophagosome and the vacuole in **D**. **F)** Schematic representation of the morphologies observed at Atg39-hfYFP foci, which are classified by number for quantification.

G) Bar graph of the number of tomograms with observed morphologies in WT and *dnm1Δ* cells categorized using schematic in **F**. Dashed lines indicate the observation of phagophore membranes.

H) Scatter plot of INMDV diameters in each morphological category described in **F** in WT and *dnm1Δ* cells. For category 1, *n*=20 vesicles in WT and *n*=17 vesicles in *dnm1Δ* cells. For category 2, *n*=6 vesicles for WT and *n*=8 vesicles for *dnm1Δ* cells. For category 3 *n*=4 vesicles for WT and *n*=1 vesicle for *dnm1Δ* cells. For category 4 *n*=4 vesicles for WT. Unpaired t test, ****$P<0.0001$; *ns*, not significant.

4B, see 3D model) while some appeared in the cortical ER proximal to the plasma membrane (Figure S4C). The observation of INMDVs confirmed that INM fission occurs prior to ONM fission (Model 1; Figure S1A). Of additional interest, INMDVs at the NE were associated with an expansion of the ONM (Figure 4A) suggesting that these events may occur alongside membrane biosynthesis and/or recruitment mechanisms. 2) There were no structures that resembled a phagophore (e.g. two ribosome-free closely apposed membranes[62]) near any Atg39-hfYFP focus that correlated to INMDVs in the NE or ER. Moreover, although 6 tomograms contained apparent NDVs that had been presumably liberated from the NE/ER (Figure 4C), only 1 of these revealed what appeared to be a phagophore in the process of engulfing the structure (Figure S4D). We did, however, observe 4 Atg39-hfYFP foci that correlated to a vesicle enclosed by 4 membranes, which we interpreted to be an NDV within an autophagosome (Figure 4D). 3) Atg39-hfYFP foci that were observed to be proximal to the vacuole by fluorescence demarked several interesting morphologies that suggest different fates for the autophagosome containing an NDV. For example, we observed close apposition/contact sites between the vacuole and autophagosome (Figure 4D; arrow, Movie 2), which was

308 evocative of a kiss and run-type mechanism that might deliver vacuolar degradative
309 enzymes in addition to the more expected direct vacuole fusion (Figure 4E). We also
310 observed Atg39-hfYFP foci that overlapped with Vph1-mCherry signal that correlated
311 with a vesicle containing membrane fragments that we presume to be derived from an
312 NDV and autophagosome (Figure S4E). 4) Lastly, we noted that the diameters of the
313 INMDVs were 25-125 nm when found within the NE/ER lumen (with a few exceptions)
314 but were 200-350 nm within NDVs in the cytosol (Figure 4H; blue dots). Making the
315 reasonable assumption that the NDVs arose from the INMDVs in the NE/ER lumen, the
316 implication is that the INMDVs may fuse together before they are released as NDVs into
317 the cytosol. Indeed, we occasionally observed multiple closely apposed INMDVs in the
318 NE/ER lumen that correlated with a single Atg39-hfYFP focus (Figure 4A, S4A)
319 including one example in which we captured two vesicles connected by a narrow
320 membrane neck as if undergoing fusion or fission (Figure S4B), further supporting this
321 idea. A clear prediction then of a model in which smaller INMDVs fuse before they are
322 liberated within a cytosolic NDV would be that larger vesicles would accumulate in the
323 NE/ER lumen upon inhibition of ONM/ER scission.

324 **Dnm1 is required for ONM/ER fission**

325 To more fully understand how Dnm1 contributes to nucleophagy, we next
326 performed CLEM to localize 29 randomly selected Atg39-hfYFP foci in the context of the
327 ultrastructure in *dnm1Δ* cells. We categorized the observed morphologies as in WT cells
328 (Figure 4F). Consistent with the idea that nucleophagy is stalled in the absence of
329 *DNM1*, we did not observe any examples of autophagosome-vacuole fusion (Category
330 4; Figure 4G; red). Instead, there was an increase in the labeling of structures that

Figure 5

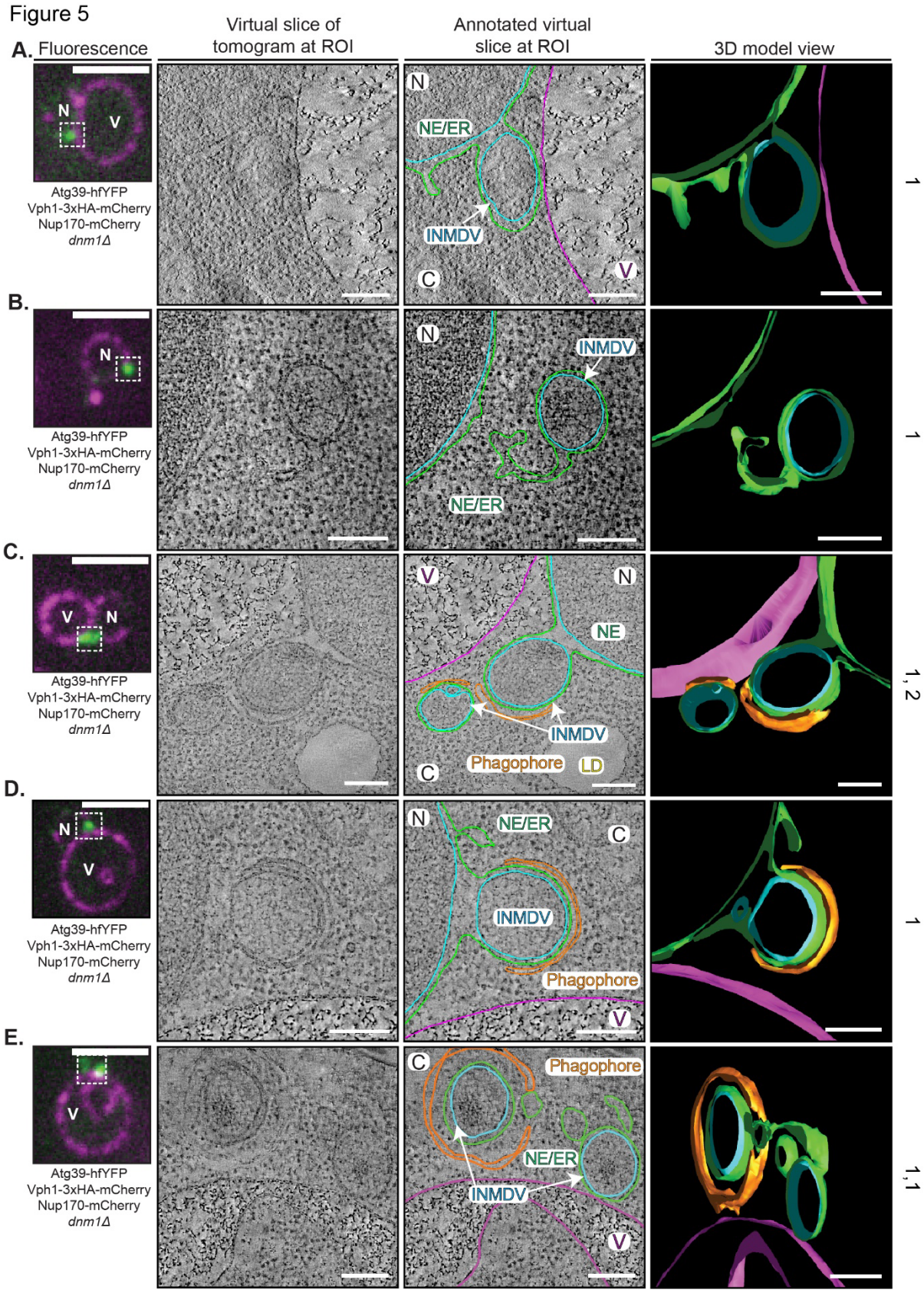
A. Fluorescence
Virtual slice of tomogram at ROI
Annotated virtual slice at ROI
3D model view
N
V
Atg39-hfYFP
Vph1-3xHA-mCherry
Nup170-mCherry
dnm1Δ
NE/ER
INMDV
C
1
B.
1
C.
NE
Phagophore
LD
1, 2
D.
1
E.
1,1

331

Figure 5 – Dnm1 is required for ONM fission.

A-E) CLEM/tomography of sites of Atg39-hfYFP foci in *dnm1Δ* cells. From left to right: fluorescence image of *dnm1Δ* cells expressing Atg39-hfYFP (green), Vph1-mCherry and Nup170-mCherry (magenta). Scale bar is 3 µm. EM tomogram acquired of boxed region in fluorescence image and tomogram virtual slice without and with annotation shown alongside a snapshot of a 3D model. Arrows point to INMDVs. ONM is green, INM is light blue, phagophore/autophagosome is orange, vacuole membrane is magenta. Scale bar is 200 nm. C, cytosol; N, nucleus; V, vacuole; NE, nuclear envelope; ER, endoplasmic reticulum; INMDV, inner nuclear membrane derived vesicle; AM, autophagic membrane. Numbers at right refer to classification scheme in Figure 4F.

332 comprise early events like those containing INMDVs within the NE/ER lumen (Figure
333 4G, Figure 5A,B, Figure S5A,B; Category 1). Most strikingly, unlike in WT cells where
334 we never observed engagement of phagophores with Atg39-hfYFP positive
335 morphologies that labeled INMDVs in the NE/ER, a quarter of category 1 tomograms
336 had double membranes that appeared as ribbons in the 3D segmentation of the whole
337 tomogram volume that were in close apposition to and followed the contour of the ONM
338 (Figure 5C-E, Figure S5C, Movie 3). In several examples as in Figure 5D and 5E, the
339 phagophores surrounded (but failed to fully encompass) the NE/ER-derived
340 membranes. Indeed, the phagophore rim appeared obstructed by NE/ER which would
341 need to be cleared by a membrane fission mechanism for phagophore closure to occur.
342 Consistent with this interpretation, we only observed a single Atg39-hfYFP focus within
343 a fully sealed autophagosome in this dataset (Figure 4G). Interestingly, we also
344 observed a four-fold increase in structures we identified as NDVs surrounded by
345 phagophores in *dnm1Δ* cells compared to WT cells (Figure 4G, Figure S5D), although
346 we think that it is likely that at least some of these structures are category 1 but are
347 miscategorized because their NE/ER connections are outside of the tomogram
348 volumes.

349 Additional evidence for stalling of nucleophagy at a step where membrane fission
350 mechanisms must be invoked is also apparent in the sizes of the INMDVs in *dnm1Δ*

351 cells. Indeed, although in WT cells INMDVs within the NE/ER lumen tend to be 25-125
352 nm in diameter (Category 1; Figure 4H), they were significantly larger (from 100-400
353 nm; Figure 4H; red dots) in *dnm1Δ* cells and resembled those that were found only in
354 WT cell NDVs, i.e. after they had been released from the NE/ER. These data thus
355 suggest that a delay in an ONM fission mechanism would allow the buildup of additional
356 membrane and perhaps cargo in the INMDV. Such an idea is also supported by the
357 observation that there is a higher copy number of Atg39-GFP within individual foci in
358 *dnm1Δ* cells (Figure 3D). Thus, we conclude that Dnm1 executes ONM fission.
359

360 **Discussion**

361 We have determined the kinetic, molecular, and morphological events that
362 comprise selective Atg39-mediated nucleophagy in budding yeast that is summarized in
363 in Figure S6A,B. Although there may be upstream events that are so far undetected at
364 the molecular and ultrastructural levels, our analysis of Atg39 localization suggests that
365 nucleophagy is mechanistically distinct from ER-phagy and occurs in three phases
366 characterized by increasing mobility of Atg39 (Figure 3E and Figure S6B). The first
367 phase, during which INM cargo is likely captured (Figure S3D,E), begins with rapid
368 (~50-100 molecules/min) local accumulation of Atg39 at a site adjacent to the NVJ. After
369 around three minutes, Dnm1 is recruited to sites of Atg39 accumulation and likely
370 severs the ONM to release an NDV into the cytosol, initiating the second phase (Figure
371 2D,E, Figure S2C, Figure 3G). Once the NDV is fully encapsulated by an
372 autophagosome, the outer membrane of the autophagosome fuses with the vacuole
373 allowing delivery of the Atg39-containing NDV. The entire process occurs in

374 approximately 5 minutes (Figure 3F), and we estimate, based on the surface area of
375 INM that is captured in the INMDVs and the rate of nucleophagy (1.4/cell/hour), that
376 ~80% of the INM is recycled over a 24-hour period when cells are starved of nitrogen.
377 Thus, nucleophagy may help rejuvenate the INM.

378 Nucleophagy incorporates two independent and sequential membrane fission
379 reactions executed by two machineries, the first acting at the INM that likely requires the
380 lumenal amphipathic helices of Atg39[30], and the second at the ONM. Our data strongly
381 implicate Dnm1 as a key player in ONM fission. This conclusion is supported by several
382 data including the robust association of Dnm1 with Atg39-containing structures (Figure
383 2) and the buildup of likely stalled nucleophagy intermediates at the NE in *dnm1Δ* cells
384 (Figure 3-5). Interestingly, however, although we observe that all Atg39 NE foci are
385 competent to recruit Dnm1 (Figure 2), the deletion of Dnm1 only leads to a ~30%
386 reduction in nucleophagic flux (Figure 1) and the stalling of ~32% of all nucleophagy
387 events (Figure 3). These data suggest that there are compensatory or redundant ONM
388 fission mechanisms, which may incorporate another dynamin-like protein or other yet to
389 be defined factors. Alternatively, it is possible that a pool of Atg39 is delivered to the
390 vacuole through Dnm1-independent routes like PMN or ER-phagy, even as our data do
391 not indicate a key role for these mechanisms in the autophagic flux of Atg39 (Figure 1).

392 Unlike PMN and ER-phagy factors that do not impact nucleophagic flux, we find
393 that Atg11 contributes to Atg39 degradation in at least two ways. First, Atg11 contributes
394 to the local NE clustering of Atg39 (Figure 1E). Such a mechanism is consistent with
395 Atg11's function as a scaffold that contributes to Vac8 clustering on the vacuolar
396 membrane, which helps form the pre-autophagosome structure (PAS) during selective

397 forms of autophagy[63]. In fact, it is possible that the local accumulation of Atg39 at the
398 NE proximal to the NVJ reflects the engagement of Atg11 with Atg39 and the PAS
399 during these early events. Second, Atg11 is required for the recruitment of Dnm1 to
400 Atg39-containing structures (Figure S2D,E) at the NE, mirroring its function at
401 mitochondria[55].

402 Unlike Atg11, Atg8 and the phagophore do not contribute to early nucleophagy
403 events associated with NE remodeling. Indeed, we do not observe any phagophore
404 engagement with the NE except under scenarios in which Dnm1 is inhibited and
405 nucleophagy is stalled after INM fission. In the latter case, the phagophore is competent
406 to enrobe the ONM but is unable to close likely due to steric hindrance imposed by the
407 continuity of the ONM (Figure 5C-E, S5C). These data suggest a tight coupling between
408 Dnm1 function and phagophore engagement, which may be a key regulatory step in
409 nucleophagy. Indeed, the data hint that Dnm1 may (either directly or indirectly) inhibit
410 phagophore engagement until it has completed ONM fission. As Atg39 has an Atg8-
411 interacting motif (AIM) that is thought to directly engage Atg8 on the phagophore[27], it will
412 be interesting to understand how and when this AIM is available for Atg8 binding and
413 the role of Dnm1 and other factors in this mechanism.

414 Future work will also need to understand the regulation of the Dnm1 fission
415 mechanism itself. The data indicate that Atg39 is released from the nucleus after around
416 100 seconds of a rapid increase in Atg39 copy number at an NE focus, which peaks at
417 ~300 molecules (Figure 3D). As the copy number is stable after it is released from the
418 nucleus (until its vacuolar degradation), we surmise that Dnm1 can act once a critical
419 threshold copy number of Atg39 is reached. Further, if we impose a correlation between

420 Atg39 copy number and INMDV size (with the consideration that INMDVs within the
421 NE/ER lumen are typically small, from 50-100 nm with only a handful at 300 nm (Figure
422 4H)), a reasonable conclusion is that Dnm1 acts once the INMDVs reach ~200-300 nm
423 in diameter, well within the experimentally-determined size of cytosolic NDVs (250 nm).
424 Such a conclusion is also supported by the observation that we only observe larger
425 diameter INMDVs stuck at the NE when ONM fission is inhibited (Figure 4H). Thus,
426 future studies will be needed to explore whether there is a threshold of Atg39 copy
427 number and/or INMDV size that serves as a trigger for Dnm1 fission, which would then
428 license phagophore engagement and ultimate closure.

429 That ONM fission may only occur once an INMDV reaches a certain size raises the
430 question of the mechanism of INMDV growth. Indeed, as there appears to be a
431 progression from 50-100 nm to much larger 200-400 nm diameter vesicles in the NE/ER
432 lumen, we must entertain the possibility that these vesicles enlarge by INMDV fusion
433 with the caveat that we cannot fully rule out that we failed to discover the fate of the
434 smaller vesicles. Although direct evidence for INMDV fusion is scant, one could interpret
435 the quanta-like merging of Atg39-GFP foci during Atg39 growth within such a framework
436 (Figure S3A). Further, we observed one example of what appeared to be two INMDVs
437 fusing (Figure S4B). As we expect INMDV fusion to be a short-lived event, even
438 capturing this single snapshot speaks to its potential prevalence. How INMDV fusion is
439 achieved is a mystery but would almost certainly require a protein fusogen on the
440 lumenal face of the vesicle membrane. Should such a fusogen exist, one must then
441 consider that INMDVs could also fuse back to the INM or with the ONM or ER
442 membranes. This idea is particularly interesting in the context of so-called NE

443 budding/egress pathways where nuclear cargo (e.g. viruses[64] or large
444 ribonucleoproteins[65]) are packaged into lumenal vesicles that then fuse with the ONM to
445 allow for their cytosolic delivery. As an extension of this idea, our observation that
446 INMDVs are found throughout the ER (even out into the cortical ER, Figure S4C)
447 suggests that this pathway may deliver nuclear components to distant regions of the cell
448 by taking advantage of the continuity of the ER network. While highly speculative,
449 INMDVs have been observed in many different contexts[66], yet their function remains
450 poorly understood often because they are not associated with any molecular signature.
451 Here, we have firmly established that at least some INMDVs are products of a
452 nucleophagy mechanism – that we have a molecular handle with Atg39 opens exciting
453 new vistas to discover the full spectrum of the role of INMDVs in NE homeostasis and
454 beyond.

Acknowledgments

We thank the Center for Cellular and Molecular Imaging for assistance with electron microscopy, particularly M. Graham, Z. Zuo, and X. Liu. This work was funded by the following grants from National Institutes of Health (NIH): R56 AG071201 and R21 AG058033 to C.P.L. and T.J.M.; R01 GM105672 to CPL; F32 GM139285 to N.R.A.; F31 AG069490 to P.J.M.

Author Contributions

Conceptualization: P.J.M., C.P.L.; Methodology: P.J.M, A.P., I.S., N.R.A., L.S.; Investigation: P.J.M., A.P., I.S., N.R.A.; Validation: P.J.M., A.P.; Data curation: P.J.M., A.P., I.S., N.R.A.; Formal Analysis: P.J.M., A.P., I.S., N.R.A.; Funding acquisition: P.J.M., T.J.M., C.P.L.; Visualization: P.J.M., A.P.; Project administration: P.J.M., M.C.K., C.P.L.; Resources: L.S., C.P.L.; Software: A.P., I.S., L.S.; Supervision: T.J.M., M.C.K., C.P.L.; Writing – original draft: P.J.M., C.P.L.; Writing – review and editing: All authors

Competing interests

The authors have no competing interests to declare.

471 **Materials and Methods**

472 ***Yeast culturing conditions and autophagy induction***

473 All experiments were performed at 30°C. Budding yeast (*S. cerevisiae*) were
474 cultured in YPA (1% Bacto-yeast extract (Y), 2% Bacto-peptone (P), 0.025% adenine
475 hemi-sulfate (A; Sigma)) supplemented with 2% glucose (D; Sigma) or in csm (complete
476 supplement mixture; Sunrise Science Products) to maintain selection for centromeric
477 plasmids. For one experiment, we used S. pombe strain MKSP3186, which was
478 cultured overnight in YE5S (yeast extract (YE), 250 mg/L adenine, histidine, leucine,
479 uracil, and lysine hydrochloride).

480 To induce autophagy by nitrogen starvation, cells in log phase were washed and
481 resuspended in synthetic defined medium lacking nitrogen (sd-N) (0.17% Difco Yeast
482 Nitrogen Base without amino acids and ammonium sulfate, and 2% D). Samples were
483 collected at time points indicated in the figures and were prepared for extraction of RNA,
484 fluorescence microscopy, or immunoblotting as described below.

485 To induce autophagy by inhibiting Tor1 kinase by treatment with rapamycin,
486 rapamycin (in DMSO; Sigma-Aldrich) was added to cells in log phase to a final
487 concentration of 250 ng/mL. Samples collected at time points indicated in the figures
488 were prepared for extraction of RNA for RT-qPCR.

489

490 ***Yeast strain construction***

491 All strains used in this study are listed in Supplementary Table 1. PCR-based
492 methods[67] using the pFA6a[68] and pK3F[69] plasmid series as templates were used to

493 generate genomic integration cassettes of sequences encoding fluorescent protein
494 genes and to delete ORFs at the genomic loci[70]. To generate PMCPL576, the *mEGFP*
495 gene followed by a kanamycin resistance cassette (*KAN-MX6*) flanked by loxP sites
496 was amplified from pPM09 using primers with homology arms that are complementary
497 to flanking sequences of the region targeted for genomic insertion. The PCR product
498 was transformed into W303A and kanamycin-resistant colonies were selected. A colony
499 containing the *KAN-MX6* cassette integrated into the proper location as assessed by
500 PCR of genomic DNA was transformed with the centromeric plasmid pSH47[71] that
501 expresses the Cre recombinase under the control of a galactose-inducible (*GAL1*)
502 promoter. Transformants were selected on csm plates lacking uracil (ura). Overnight
503 cultures of individual colonies grown in csm -ura supplemented with 2% raffinose were
504 diluted into csm -ura supplemented with 2% galactose to induce the expression of the
505 Cre recombinase for 5 hours before single cells were plated on YPD. Colonies were
506 screened for loss of *KAN-MX6* by testing growth on geneticin (Thermo Fisher
507 Scientific)-containing plates; the expression of *ATG39-mEGFP* was confirmed by
508 fluorescence microscopy and immunoblot. PMCPL578, PMCPL1257, PMCPL1045, and
509 PMCPL1097 were generated in a similar manner using pPM26, pPM31, pPM28, and
510 pPM27 respectively as PCR templates.

511 Genomic integration of *DNM1* and *dnm1 K41A* genes (PMCPL1319,
512 PMCPL1087, PMCPL1112, and PMCPL1113) were generated by genomically
513 integrating linearized pPM11 and pPM15 at the *URA3* gene.

514

515 ***Plasmid generation***

516 All plasmids used in this study are listed in Supplementary Table 2. All DNA
517 fragments used for cloning were purified using a gel purification kit/protocol (Qiagen). All
518 PCR was performed using KOD polymerase (EMD Millipore). To generate pPM09,
519 pPM27, and pPM32, the *mEGFP*, *pHlourin*, and *mCherry* ORFs were amplified by PCR
520 using pFa6a-mEGFP-kanMX6 (a gift from Julien Berro[72], Addgene plasmid # 87023),
521 pAS1NB (a gift from Mark Prescott[35], Addgene plasmid # 71245), and pFa6a-3xHA-
522 mCherry-natMX6, respectively. The amplicons were then assembled into pK3F
523 (linearized with *Spe*I (New England Biolabs)) using the Gibson Assembly Master Mix
524 (New England Biolabs). pPM28 was similarly generated by Gibson Assembly of the
525 *pHlourin* amplicon into pPM32. To generate pPM31, the ORF for *hfYFP*[61] was yeast
526 codon optimized using the codon optimization tool from IDT and synthesized as a g-
527 block flanked by *Spe*I restriction enzyme recognition sites (IDT). The g-block was
528 solubilized in TE and Gibson Assembled into pK3F as described above. To generate
529 pPM29, an amplicon containing the *HEH1* promoter, the coding sequence of a fragment
530 of Heh1 encoding the first 479 amino acids, followed by the *ADH1* 3'UTR, was amplified
531 by PCR using genomic DNA from PMCPL1082 as a template and primers with *Eag*I and
532 *Xho*I restriction enzyme recognition sites. The amplicon was restriction digested with
533 *Eag*I (New England Biolabs) and *Xho*I (New England Biolabs) and ligated (T4 DNA
534 ligase, Invitrogen) into pRS405 digested with *Eag*I and *Xho*I. To generate pPM30, an
535 ORF containing the mCherry coding sequence was generated by PCR using pSJ1321
536 (a gift from Sue Jaspersen[73], Addgene plasmid #86413) as a template and primers with
537 *BamH*I and *Pac*I restriction enzyme recognition sites. The amplicon was restriction

538 digested with *BamH*I (New England Biolabs) and *Pac*I (New England Biolabs) and
539 ligated into gel purified pPM29 digested with *BamH*I and *Pac*I.

540 pPM03 was generated in two steps. First, the genomic region containing the
541 *ATG8* promoter (576 base pairs immediately upstream of the *ATG8* start codon) was
542 generated by PCR using genomic DNA from W303A and primers with *Sac*I and *Eag*I
543 restriction enzyme recognition sites. The amplicon was restriction digested with *Sac*I
544 (New England Biolabs) and *Eag*I ligated into pRS406 linearized with *Sac*I and *Eag*I.
545 Next, the genomic region containing the *ATG8* terminator (319 base pairs immediately
546 downstream of the *ATG8* stop codon) was generated in a similar manner using primers
547 with *Hind*III and *Sal*I restriction enzyme recognition sites. The amplicons were digested
548 with *Sac*I and *Eag*I ligated into the plasmid containing the *ATG8* promoter linearized
549 with *Hind*III (New England Biolabs) and *Sal*I (New England Biolabs). To generate
550 pPM11, the *DNM1* gene was amplified by PCR using genomic DNA from W303A and
551 primers with *Eag*I and *Spe*I restriction enzyme recognition sites. The amplicon was
552 restriction digested with *Eag*I and *Spe*I and ligated into pPM03 linearized with *Eag*I and
553 *Spe*I.

554 To generate pPM15, site-directed mutagenesis of the codon encoding lysine at
555 amino acid position 41 was altered to alanine using the Q5 site-directed mutagenesis kit
556 (New England Biolabs) using pPM11 as a template. All plasmid sequences were
557 confirmed by Sanger sequencing.

558

559 ***RTqPCR***

560 RNA extraction was performed using the MasterPure Yeast RNA purification kit
561 (Lucigen) from samples treated as indicated in the legend of Figure S1. cDNA was
562 produced from ~1 µg of RNA using M-MuLV Reverse Transcriptase (New England
563 Biolabs). RTqPCR was performed on 1:10 dilutions of the cDNA using iTaq Universal
564 SYBR Green Supermix (Bio Rad) and primer pairs validated for RTqPCR efficiency for
565 *ATG39* (sATG39 qPCR 6 and asATG39 qPCR 6), *ATG8* (sATG8 qPCR and asATG8
566 qPCR), *ATG11* (sATG11 qPCR and asATG11 qPCR), *ATG40* (sATG40 qPCR and
567 asATG40 qPCR), and *ACT1* (sACT1 qPCR and asACT1qPCR) which served as a
568 control. All PCRs were performed using CFX96 Touch Real-Time Detection System
569 thermocycler (BioRad). Cq values as reported by the thermocycler during the RTqPCR
570 for the gene of interest were subtracted from those of *ACT1* to obtain ΔCq. ΔΔCq was
571 then obtained by subtracting the ΔCq value of the control condition from the condition of
572 interest (i.e. rapamycin or nitrogen starvation). Fold change was calculated as $2^{-\Delta\Delta Cq}$.

573

574 ***Live-cell Microscopy***

575 For all live-cell imaging, cells incubated in sd-N for the duration of time indicated
576 in the figure legend were gently collected by centrifugation and resuspended in sd-N
577 prior to imaging. Images from Figure 1C, Figure S1F, Figure S2D, and the images used
578 to generate the data in Figure 3D were acquired on a DeltaVision microscope (Applied
579 Precision) equipped with a UPlanSapo x100 1.4 numerical aperture oil immersion
580 objective (Olympus), and an AURA light engine (Lumencor) and CoolSnapHQ^2 charge-
581 coupled device (CCD; Photometrics) camera imaging using an Insight SSI four-color
582 live-cell filter set (GFP: excitation, 425–495 nm and emission, 500–550 nm; YFP:

583 excitation, 496–528 nm and emission, 537–559 nm; mCherry: excitation, 555–590 nm
584 and emission, 600– 675 nm) using Resolve3D in SoftWoRx 7.0.0 software. The
585 microscope stage and objectives were maintained at 30°C within an environmental
586 chamber.

587 All other images were acquired on a lattice light sheet microscope[74] equipped
588 with a 25X 1.1 numerical aperture CFI APO LWD objective (Nikon) whose focal plane is
589 coincident with the light sheet, and a sCMOS camera (Hamamatsu Orca Flash 4.0 v2).
590 Cells were added to 5 mm round cover slips (Warner Instruments) coated with
591 Concanavalin A (Sigma) as described in[75]. The coverslip with the cells adhered was
592 then placed in an imaging chamber in a bath containing sd-N media warmed to 30°C.

593

594 ***Correlative light and electron microscopy***

595 Correlative light and electron microscopy of resin-embedded cells was performed
596 based on the protocol published by Kukulski and colleagues[76]. In brief, cells
597 (PMCPL1283 and PMCPL1390) were cultured in sd-N for four hours. Cells were
598 pelleted by centrifugation at ~800 RCF for five minutes and high-pressure frozen in the
599 200-µm recess of an aluminum platelet (Engineering Office M. Wohlwend 241) using an
600 HPM100 (Leica Microsystems). The samples were then freeze substituted in 0.1%
601 uranyl acetate. Automated temperature control was then used to complete the solution
602 exchange and embedding in Lowicryl HM20 (Polysciences). Sectioning was performed
603 using a diamond knife (Diatome) mounted on an ultramicrotome (Leica Artos 3D) to a
604 nominal thickness of 250 µm. Sections were then collected on carbon-supported 200-
605 mesh copper grids (Ted Pella 01840).

606 The position of Atg39-hfYFP was determined by fluorescence microscopy. Next,
607 15 nm protein A-coated gold beads (Cell Microscopy Core, University Medical Center
608 Utrecht) were adhered to the grids to aid in the tilt-series alignment.

609 We used automated tilt-series acquisition via SerialEM 3.6.15[77] on an electron
610 microscope (FEI TF20) operating at 200 kV from approximately -65 to +65 degrees
611 (one-degree increments) with a high-tilt tomography holder (Fischione Instruments
612 2020), a 100 µm objective aperture, a 150 µm C2 aperture, and a 4k x 4k Eagle CCD
613 (FEI) at a binned pixel size of 1.242 nm. Single- or dual-axis tilt series were acquired as
614 necessary to achieve sufficient contrast to visualize membranes. IMOD 4.11.24[78] was
615 used for reconstruction (in an automated fashion[79]), nonlinear anisotropic diffusion
616 filtering, and manual segmentation. Vph1-3xHA-mCherry and Nup170-mCherry
617 fluorescence were used to correlate fluorescence and electron microscopy images to
618 localize the Atg39-hYFP within the ultrastructure.

619

620 ***Calculating expected time resolution in observable morphological intermediates***
621 ***in CLEM***

622 A modification of the popular coupon collector's problem[80] from probability theory
623 was used to estimate the number of tomograms needed to observe all morphologies in
624 nucleophagy which persist for a given amount of time. The equation used is

627 $$\boldsymbol{E} = \frac{\boldsymbol{T}}{\Delta \boldsymbol{t}}\left(\frac{\mathbf{1}}{\mathbf{1}} + \frac{\mathbf{1}}{\mathbf{2}} + \cdots + \frac{\mathbf{1}}{\boldsymbol{T}/_{\Delta \boldsymbol{t}}}\right)$$

625 where E is the expected number of tomograms need to visualize at least one example
626 of all morphological intermediates that exist for a time (Δt) as a ratio to the average time

628 (T) Atg39- foci are outside of the vacuole (~300 seconds, Figure 3I). Using this formula,
629 we calculated that 30 tomograms were sufficient to achieve a time resolution of 30
630 seconds. Simply put, it is statistically likely to observe at least one instance of a
631 morphological intermediate in nucleophagy that is identifiable by CLEM that persists for
632 more than 30 seconds in a random selection of 30 tomograms.

633

634 ***Image processing and analysis***

635 Micrographs acquired on the Applied Precision DeltaVision microscope were
636 deconvolved using an iterative algorithm in SoftWoRx (6.5.1; Applied Precision, GE
637 Healthcare). Unprocessed images were used for all quantification of fluorescence
638 intensity on micrographs acquired on the DeltaVision. Fluorescence intensity values
639 from micrographs were measured in FIJI/imageJ[81]. Micrographs acquired on the LLSM
640 were deskewed and deconvolved as described in[74]. LLSM images were rendered in 3D
641 (Figure 3A and 3B) using the commercial software Imaris (Oxford Instruments).

642

643 ***Nucleophagy flux calculations***

644 Cells expressing Atg39-pHlourin-mCherry (PMCPL1045, PMCPL1078,
645 PMCPL1079, PMCPL1253, PMCPL1130, PMCPL1282, PMCPL1066, PMCPL1249,
646 PMCPL1276, PMCPL1243, PMCPL1252, PMCPL1264, PMCPL1067, PMCPL1127,
647 PMCPL1293, PMCPL1274, PMCPL1124) were cultured overnight, incubated in sd-N
648 media for 6 hours, and prepared for imaging on the DeltaVision. To calculate
649 nucleophagy flux, all the Atg39-pHlourin-mCherry foci in the cell were manually counted

650 and the number of red-only foci was divided by the sum of the red-only and red/green
651 foci. The ratio obtained in WT was normalized to 1 and used to compare to all other
652 genotypes.

653

654 ***NE mCherry fluorescence calculation***

655 Cells expressing Atg39-pHlourin-mCherry (PMCPL1045, PMCPL1078,
656 PMCPL1079, PMCPL1253, PMCPL1130, PMCPL1282, PMCPL1066, PMCPL1249,
657 PMCPL1276, PMCPL1243, PMCPL1252, PMCPL1264, PMCPL1067, PMCPL1127,
658 PMCPL1293, PMCPL1274, PMCPL1124) were cultured overnight, incubated in sd-N
659 media for 6 hours, and prepared for imaging on the DeltaVision. To measure NE
660 mCherry fluorescence, a 4 pixel-wide ROI was drawn along the nuclear periphery in
661 regions devoid of Atg39 fociand the mean fluorescence intensity was measured and
662 background fluorescence was subtracted.

663

664 ***Nucleophagy frequency quantification***

665 The number of Atg39-GFP accumulations in an experiment (three biological
666 replicates total) was divided by the total number of cells. The resulting number was then
667 divided by the duration of the experiment to obtain the number of nucleophagic
668 events/cell/hour.

669

670 ***Determining Atg39-GFP copy number***

671 Atg39-GFP expressing cells (PMCPL940, PMCPL856) were incubated in sd-N
672 media for four hours prior to imaging and each were separately mixed with Fta3-GFP
673 expressing cells (MKSP3186) and mounted onto coverslips. Raw images were then
674 analyzed using a custom-written MATLAB function, 'findIrregularSpots3' described
675 previously[57] that finds fluorescent objects regardless of their shape and returns xyz-
676 coordinates of the object centroids. The xyz coordinates were then used as inputs for a
677 custom-written MATLAB function 'fitSpots3' to fit and compute the volume of a 2D
678 Gaussian to a Z-slice image closest to the z-coordinate of the spot centroid. Fta3-GFP
679 spots were manually curated for their position in the cell cycle and those that were
680 determined to be in anaphase B were selected for analysis. Atg39-GFP copy number
681 was estimated by dividing the Gaussian volume for each spot by the average Gaussian
682 volume of the Fta3-GFP spots, previously calculated to be 111 molecules[60].

683

684 ***Particle tracking/colocalization***

685 Cells (PMCPL940, PMCPL857, PMCPL831, PMCPL1319, PMCPL1087) were
686 incubated in sd-N media for three hours before being prepared for imaging on the
687 LLSM. Cells where a Atg39-GFP focus appeared that underwent nucleophagy were
688 selected for further processing using MATLAB scripts to detect Atg39-GFP foci (spots)
689 as described in "Determining Atg39-GFP copy number." For particle tracking and
690 colocalization analysis the spots were organized into trajectories using previously
691 described MATLAB implementation[58] of the widely-used tracking algorithm 'track.m'[59].
692 Trajectories of a single Atg39-GFP spot that were erroneously split in two (when
693 displacement between two frames exceeded a maximum linking distance) were linked

694 together manually. For the relative Gaussian volume analysis, Gaussian volumes were
695 calculated from Atg39-GFP spots as described above. The Gaussian volume of the
696 tracked spot was normalized to that of the first time point in the trajectory. The spot
697 coordinates in each track were also used to calculate displacement of Atg39-GFP
698 between frames using a custom Jupyter Notebook script, implemented in Python
699 (Figure 3E,G, Figure S2C).

700 For colocalization analysis, a custom Jupyter Notebook Python script used the
701 coordinates of the identified Dnm1-mCherry spots which correspond to the time points
702 of the Atg39-GFP tracks to calculate the distance from the center of the Atg39-GFP
703 spots to the center of the closest Dnm1-mCherry spot (Figure 2D,E, Figure S2A,B).
704 Colocalization was considered as a distance of less than 400 nm.
705 All MATLAB and Jupyter Notebook Python script are available on GitHub: https://
706 https://github.com/LusKingLab/

707

708 ***Quantification of INMDV diameter***

709 The diameter of the INMDVs was measured in IMOD.

710

711 ***Estimation of the percentage of INM turned over by nucleophagy in 24 hours***

712 To estimate the percentage of INM that could be turned by nucleophagy in 24
713 hours, the amount of surface area of the INMDV removed in one round of nucleophagy
714 in WT cells was determined. For this, the surface area of INMDVs in category 2-4 (i.e.
715 after release as cytosolic NDVs) were approximated as ellipsoids and the length of the

716 major and minor axes were measured on IMOD. The a and b axes (major and minor
717 axes) were measured as the maximum distance within the membrane of the INMDV
718 and the distance within the membrane orthogonal to the maximum, respectively. The c
719 axis was recorded as the distance between the intersection of the major and minor axes
720 and the edge of the INMDV. The surface area was then approximated using the a, b,
721 and c radii and the ellipsoid surface area formula. The median value was then multiplied
722 by the frequency of nucleophagy (1.4 events/cell/hour) and by 24 hours to estimate the
723 surface area of the of INM removed per cell in 24 hours. This value was calculated as
724 ~7.14 μm^2. To estimate the surface area of the NE prior to nitrogen starvation, cells
725 expressing Heh1-GFP were imaged in log phase, and the radii of the nuclei were
726 measured, and the surface area was calculated using the equation for the surface area
727 of a sphere. The mean value was determined to be ~8.63 μm^2.

728

729 ***Statistical methods***

730 Graphs were generated using Prism (GraphPad 9.0). Statistical significance tests
731 were used as indicated in figure legends. Significance values were calculated within
732 Prism (GraphPad 10.0) and p-values are indicated on the graph or in figure legends as:
733 *ns*, $p > 0.05$; * $p \leq 0.05$; ** $p \leq 0.01$; *** $p \leq 0.001$; **** $p \leq 0.0001$. Error bars are
734 described in figure legends.

735

736 ***Whole cell extract preparation***

737 5 O.D. cells were pelleted by centrifugation and resuspended in 10% TCA for 1 h
738 on ice and centrifuged at 15,000 *g* for 10 min at 4°C. The pellet was washed with ice-
739 cold acetone, homogenized by sonication (Bioruptor UCD-200) and pelleted by
740 centrifugation. After two cycles of washing and sonication, the pellet was vacuum-dried
741 for 15 min. The dried cell pellet was then mechanically disrupted with 100 µl glass
742 beads (Sigma) and 100 µl 50 mM Tris-HCl pH 7.5, 8 M Urea, 2% SDS, and 1 mM
743 EDTA, followed by addition of 100 µl protein sample buffer (Tris-HCl pH 6.8, 7 M urea,
744 10% SDS, 24% glycerol, bromophenol blue, and 10% β-mercaptoethanol).

745

746 ***Immunoblotting***

747 Proteins from whole cell extracts were resolved on 4-20% SDS-polyacrylamide
748 gels (BioRad), followed by transfer of the proteins to 0.2 µm nitrocellulose membranes
749 (Bio-Rad). The membranes were blocked in 5% non-fat milk in TBST for 1 h and
750 immunoblotted with an antibody against HA directly conjugated to HRP (anti-HA-HRP;
751 Roche) for 1 h at room temperature. Blots were visualized by ECL (Thermo Fisher
752 Scientific) using a VersaDoc Imaging System (BioRad). Relative protein loading was
753 visualized using Ponceau S Solution (Sigma).

754

755 **Supplemental Figures**

Figure S1

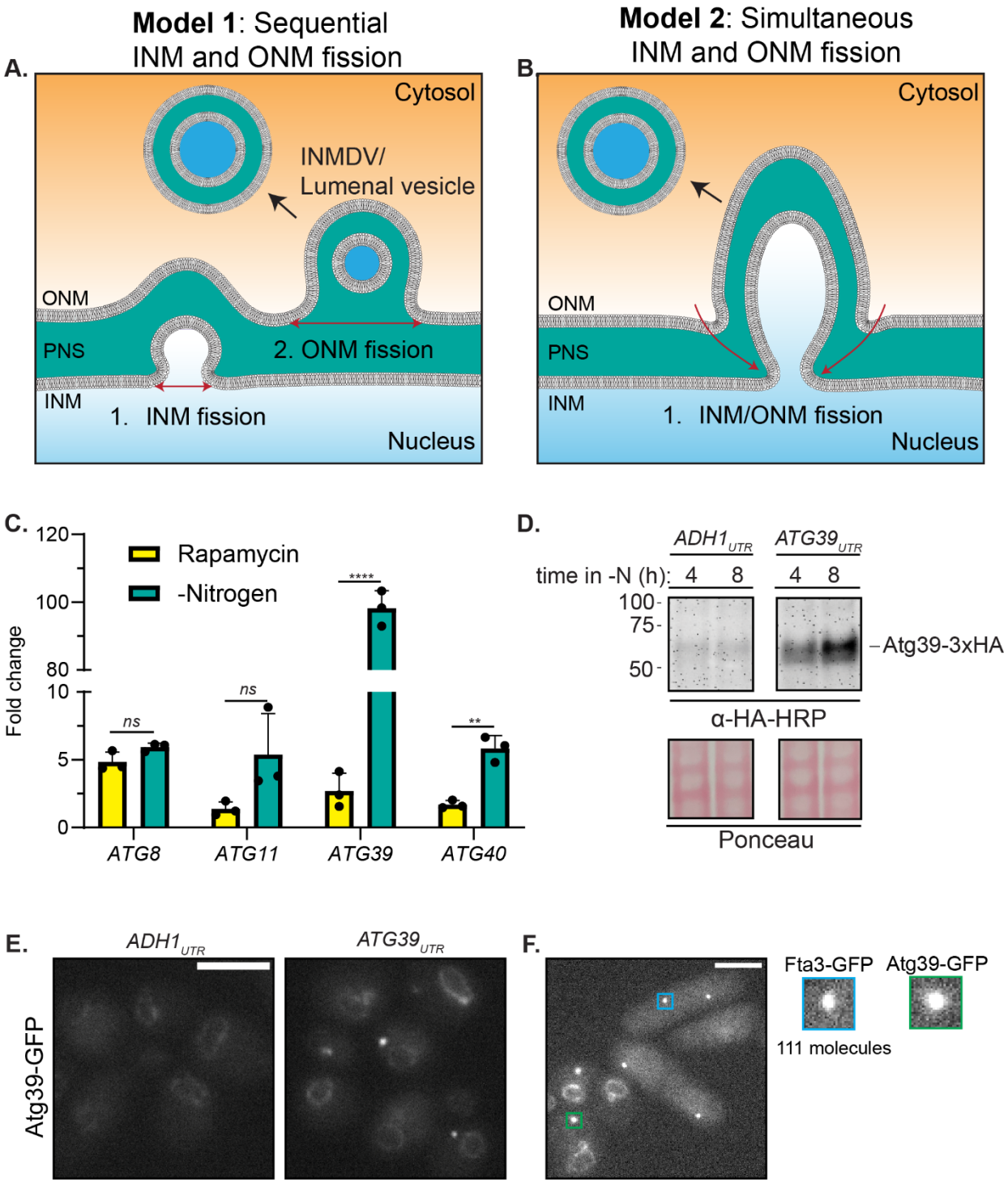

Supplemental Figure 1 – Models of nucleophagy and characterization of Atg39 expression and copy number.

A) Schematic of two models of nucleophagy incorporating either sequential (Model 1) or simultaneous (Model 2) INM and ONM fission events. Model 1 would also lead to the formation of a lumenal vesicle/INMDV intermediate. ONM, outer nuclear membrane; INM, inner nuclear membrane; PNS, perinuclear space; INMDV, inner nuclear membrane-derived vesicle; NDV, nucleus-derived vesicle.

B) RTqPCR on indicated autophagy gene transcripts was performed in WT cells either treated with rapamycin for 2 h or cultured in medium lacking nitrogen for 2 h. Results displayed as a bar graph comparing the mean fold change of the transcripts between the rapamycin and -Nitrogen condition. Mean and standard deviation (error bars) of three biological replicates (black dots). Unpaired t test. ****P<0.0001; **P<0.01; *ns*, not significant.

C) Protein levels of Atg39-3xHA fusions derived from transcripts including either the *ADH1* 3'UTR or the endogenous *ATG39* 3'UTR were assessed by Western blot with anti-HA antibody directly coupled to HRP (α-HA-HRP) and ECL. Positions of molecular weight standards (kD) at left. Membranes were stained with Ponceau to evaluate total protein loads.

D) Fluorescent micrographs of Atg39-GFP produced from transcripts with 3'UTRs from the *ADH1* or *ATG39* genes after 4 h in medium lacking nitrogen. Scale bar is 5 µm.

E) To calculate copy number of Atg39-GFP within individual foci, we imaged budding yeast expressing Atg39-GFP next to *S. pombe* expressing Fta3-GFP, a kinetochore protein which has 111 molecules/focus in anaphase B[57]. By directly relating the fluorescence intensities, we calculated Atg39-GFP copy number/focus as presented in Figure 3D.

756

Figure S2

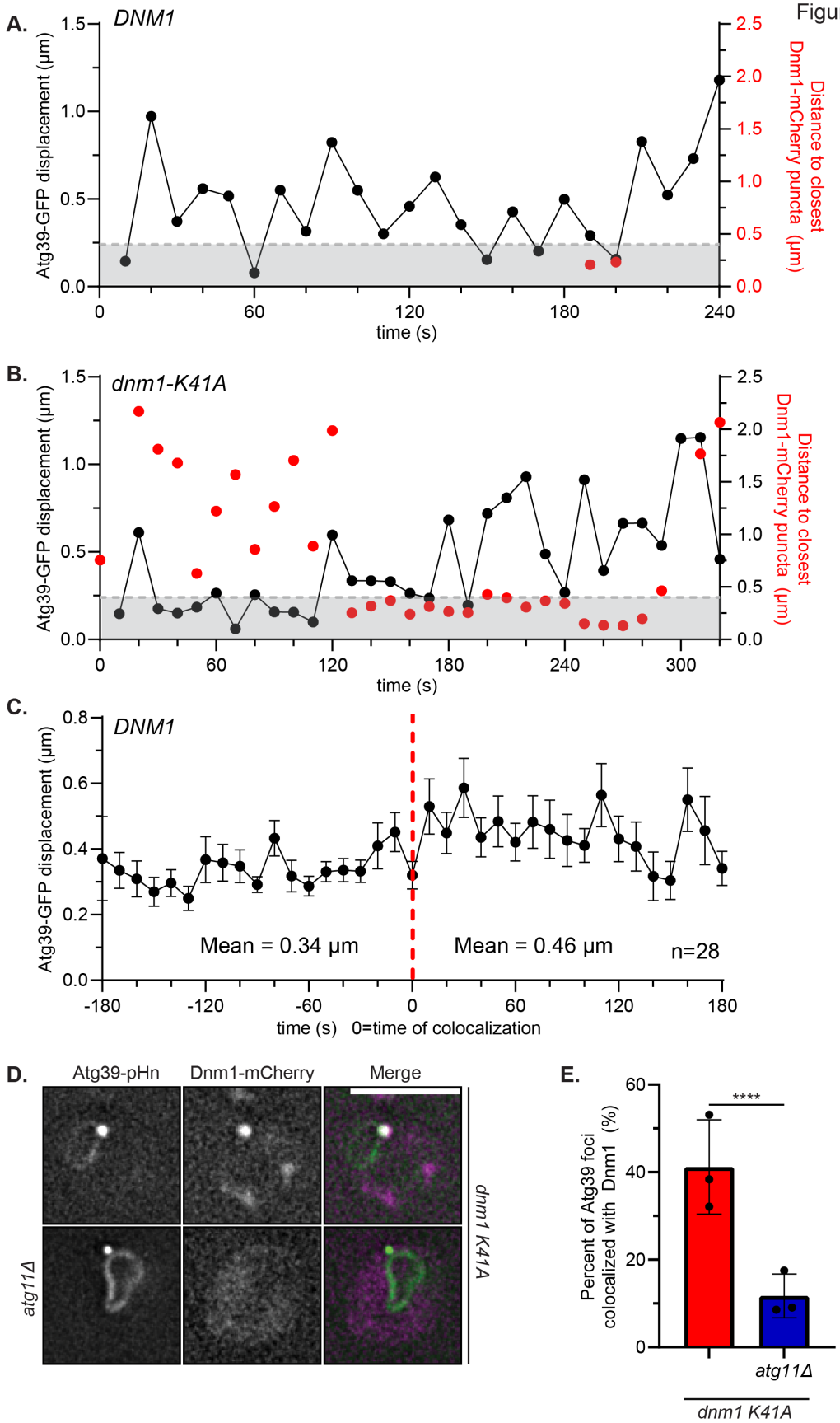

757

Supplemental Figure 2 – Dnm1 colocalizes with Atg39 in an Atg11-dependent manner.

A) Plot of the displacement (μm) of a single Atg39-GFP focus (from Figure 2A) every 10 s through a timelapse image series of *fis1Δ* cells expressing an extra copy of *DNM1*. At each time point the distance from the Atg39-GFP position to the nearest Dnm1-mCherry focus is also plotted (red axis/red dots). Colocalization was determined to be within 400 nm (grey shaded area). Note that Dnm1-mCherry only appears in two frames in the timelapse where it colocalizes with Atg39-GFP.

B) As in A, but in the context of the *dnm1-K41a* allele.

C) A line plot depicting the average mobility of Atg39-GFP foci before and after the first instance of colocalization (synchronized as time 0) with Dnm1-mCherry in *fis1Δ* cells expressing an extra copy of *DNM1*. The average displacement of all time points before and after colocalization is indicated. *n*=26 tracks from 26 cells in which colocalization between Atg39-GFP and Dnm1-mCherry was observed. Mean and SEM are plotted.

D) Fluorescent micrographs of *fis1Δ* cells and *fis1Δ atg11Δ* cells expressing Atg39-pHluorin, Dnm1-mCherry and the dnm1-K41A allele under conditions of nitrogen starvation. Green and red channels with merge are shown. Scale bar is 5 μm.

E) Plot of the mean percentage of Atg39-GFP foci that colocalize with Dnm1-mCherry from experiments in D. Mean and standard deviation (error bars) from three biological replicates (black dots). Unpaired t test, *n*=300 cells, at least 100 per biological replicate. ****P<0.0001.

758

Figure S3

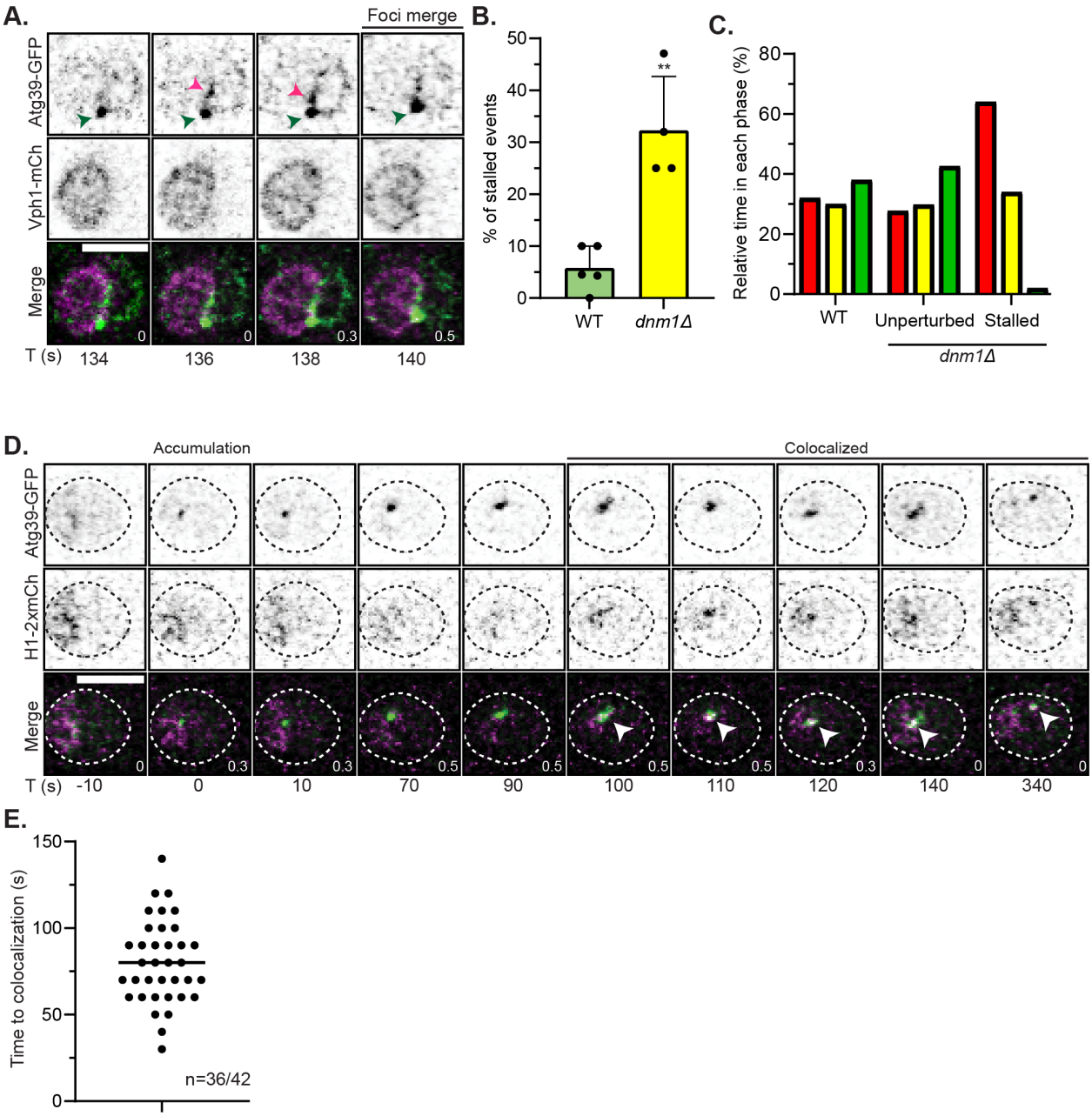

759

Supplemental Figure 3 – Characteristics of Atg39-GFP growth and mobility and cargo capture.

A) Inverted fluorescent micrographs of WT cells expressing Atg39-GFP and Vph1-mCherry (mCh) imaged every two seconds. Green and red channels and merge shown. Numbers in merge are z-position (in µm) of the displayed image in reference to the midplane. T (s) indicates the time in seconds since the first detection of the Atg39-GFP focus (green arrowhead). Another less intense focus of Atg39-GFP is visible merging with the initial particle (pink arrowhead). Scale bar is 3 µm.

B) Bar graph of the percentage of Atg39 foci tracked from first appearance that never make it into the vacuole over a 20-minute timelapse experiment as noted in Figure 3F for the indicated genotype. Mean and standard deviation (error bars) from 5 (WT cells) or 4 (*dnm1*Δ cells) biological replicates (black dots). Unpaired t test, *n*=114 tracks, 99 cells for WT cells and *n*=95 tracks, 82 cells for *dnm1*Δ cells. **P<0.01.

C) Plot of the relative time (as a percentage) that Atg39-GFP particles spend in each phase as per color code in Figure 3E and 3G in WT and *dnm1Δ* cells. The latter are also segregated based on those that enter the vacuole (unperturbed) and those that don't (stalled).

D) Inverted fluorescent micrographs of WT cells expressing Atg39-GFP and a model INM cargo comprising the INM targeting and transmembrane domain of Heh1 fused to two tandem mCherry fluorophores (H1-2xmCh). Imaged every 10 seconds with time 0 assigned to the point of Atg39-GFP focal accumulation. Green and red channels shown with merge. Arrowheads point to colocalization between Atg39-GFP and H1-2xmCh. Cell boundaries are outlined. Numbers in merge are z-position (in µm) of the displayed image in reference to the midplane. Scale bar is 3 µm.

E) Scatter plot depicting the elapsed time from the first detection of an Atg39-GFP focus and the first instance of colocalization with H1-2xmCh from experiments as in D. Black bar is median.

760

Figure S4

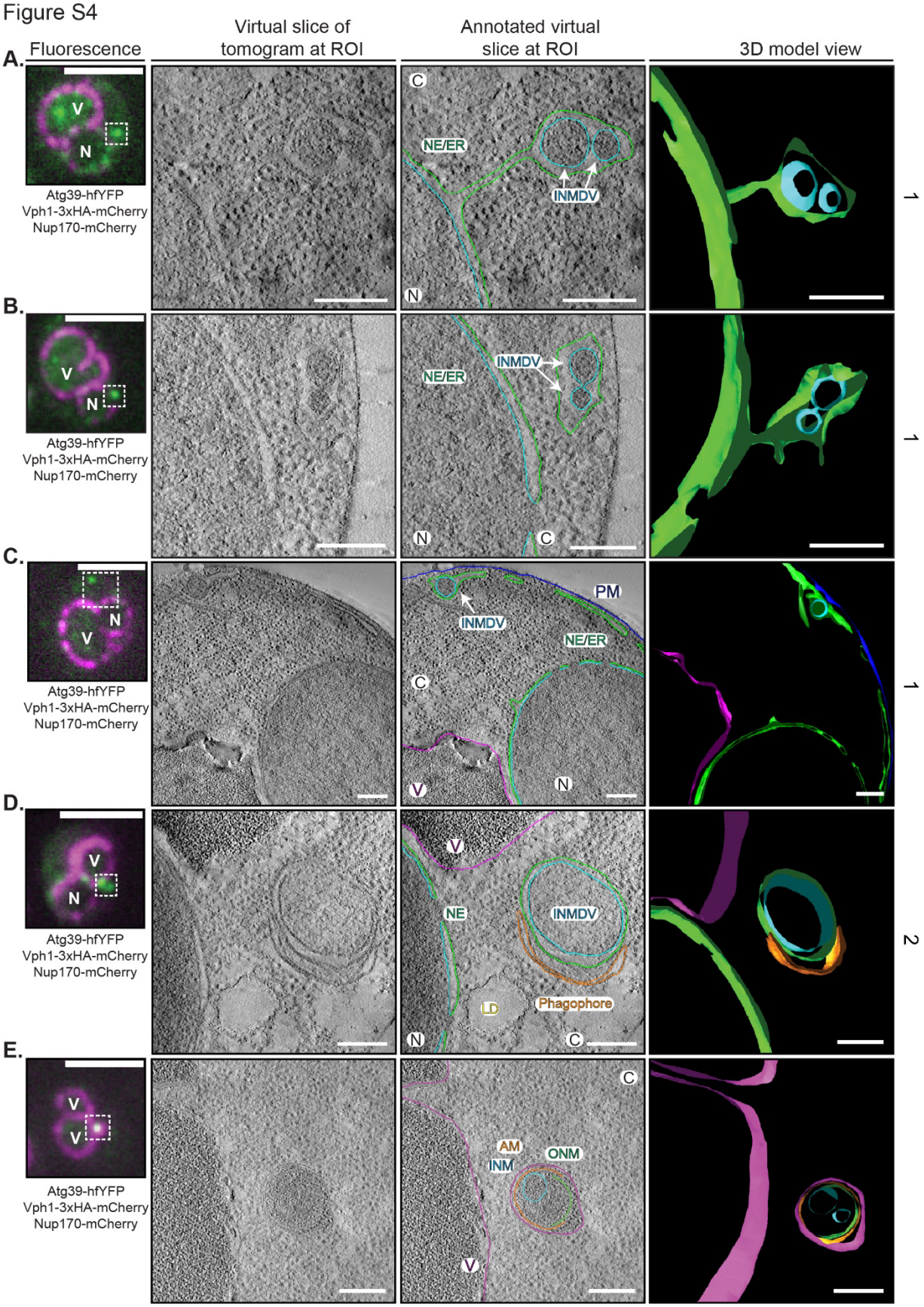

761

Supplemental Figure 4 – Ultrastructure of sites of Atg39 accumulation during nucleophagy

A-E) CLEM/tomography of sites of Atg39-hfYFP foci. From left to right: fluorescence image of WT cells expressing Atg39-hfYFP (green), Vph1-mCherry and Nup170-mCherry (magenta). Scale bar is 3 µm. EM tomogram acquired of boxed region in fluorescence image and tomogram virtual slice without and with annotation shown alongside a snapshot of a 3D model. Arrows point to INMDVs. ONM is green, INM is light blue, phagophore/autophagosome is orange, vacuole membrane is magenta. Scale bar is 200 nm. C, cytosol; N, nucleus; V, vacuole; NE, nuclear envelope; ER, endoplasmic reticulum; INMDV, inner nuclear membrane derived vesicle; AM, autophagic membrane. Numbers at right refer to classification scheme in Figure 4F.

762

Figure S5

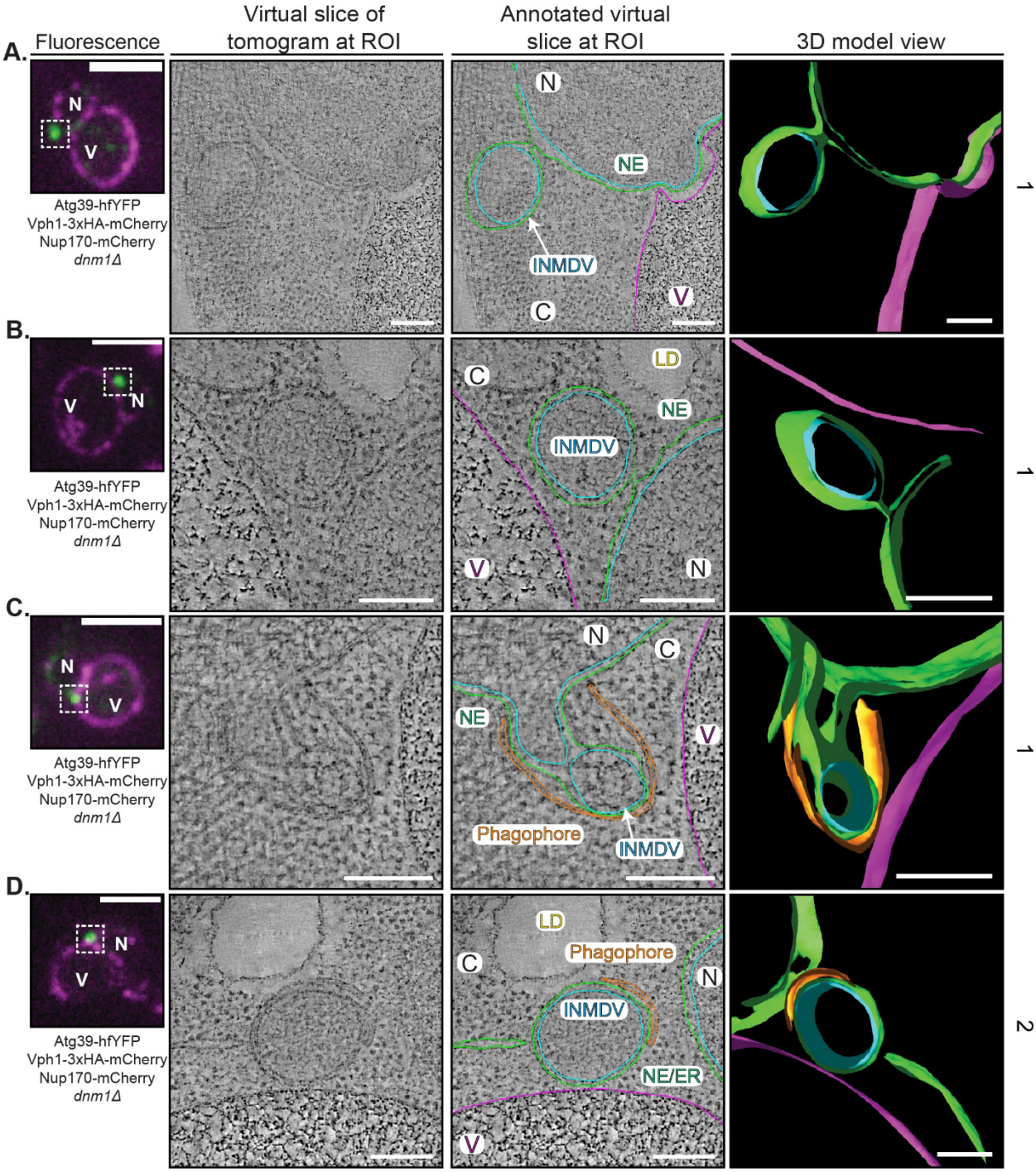

763

Supplemental Figure 5 – Ultrastructure of sites of Atg39 accumulation in *dnm1Δ* cells.

A-D) CLEM/tomography of sites of Atg39-hfYFP foci in *dnm1Δ* cells. From left to right: fluorescence image of WT cells expressing Atg39-hfYFP (green), Vph1-mCherry and Nup170-mCherry (magenta). Scale bar is 3 µm. EM tomogram acquired of boxed region in fluorescence image and tomogram virtual slice without and with annotation shown alongside a snapshot of a 3D model. Arrows point to INMDVs. ONM is green, INM is light blue, phagophore/autophagosome is orange, vacuole membrane is magenta. Scale bar is 200 nm. C, cytosol; N, nucleus; V, vacuole; NE, nuclear envelope; ER, endoplasmic reticulum; INMDV, inner nuclear membrane derived vesicle; AM, autophagic membrane; LD, lipid droplet. Numbers at right refer to classification scheme in Figure 4F.

764

Figure S6

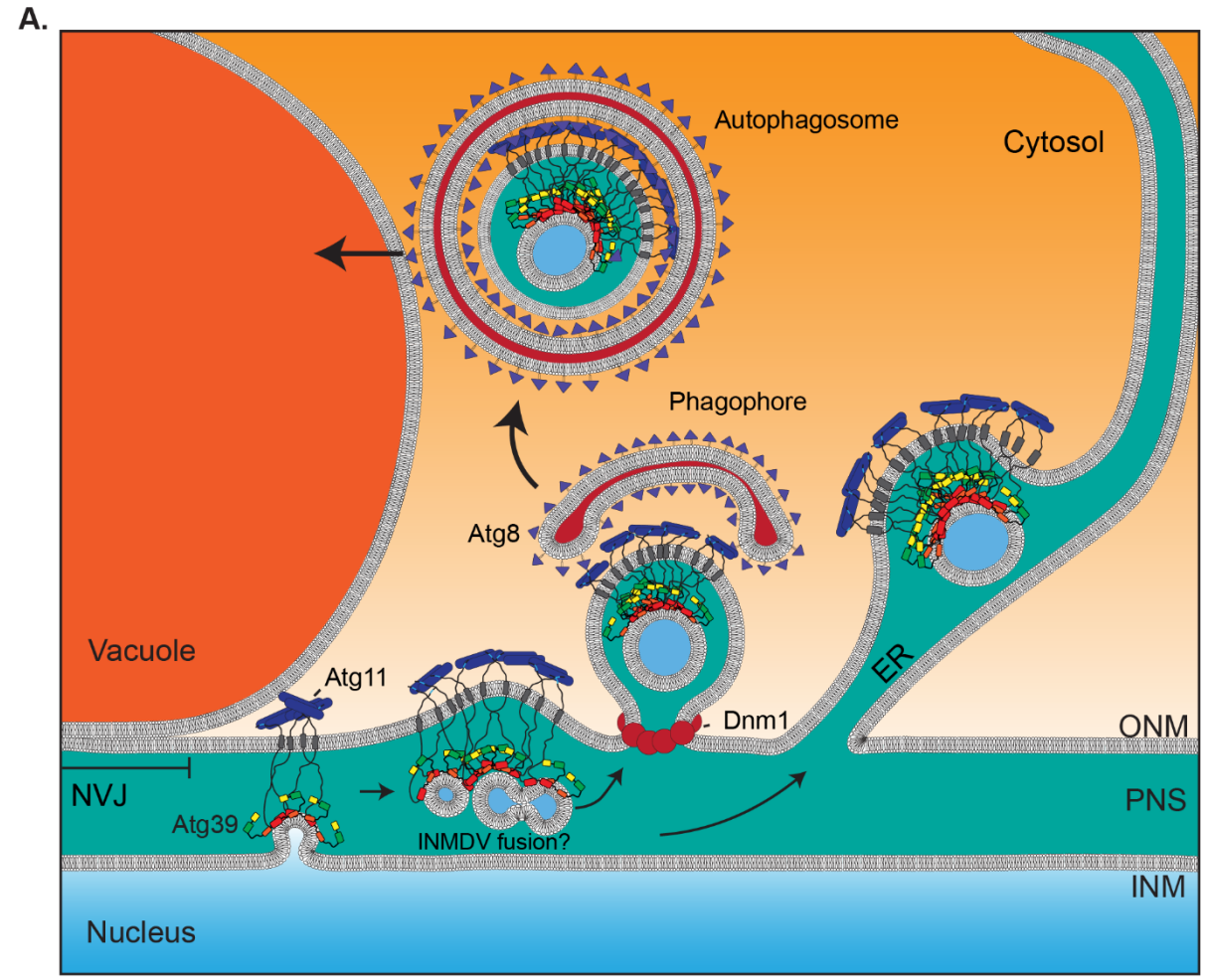

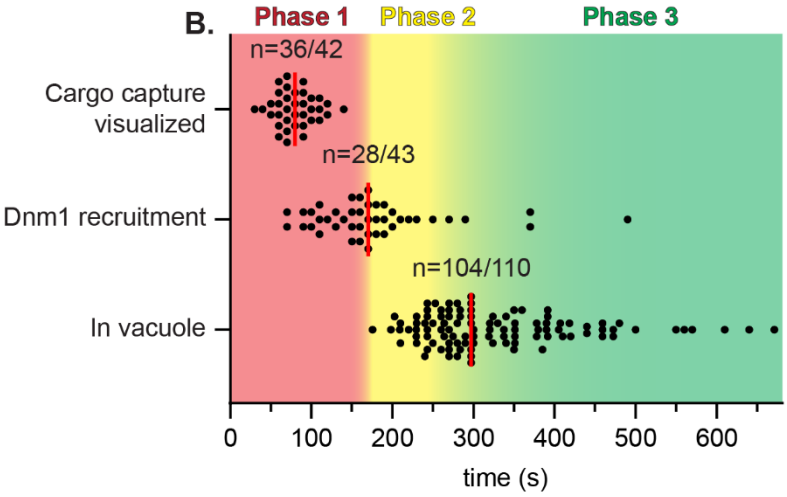

765

766

Supplemental Figure 6 – Proposed model of nucleophagy.

A) Illustrative model of the molecular and morphological steps of nucleophagy. Atg39 locally accumulates adjacent to the NVJ in a mechanism supported by Atg11 (blue cylinders). It is likely that this clustering coincides with cargo capture and the evagination and fission of the INM to generate an INMDV. Initial small (50-100nm INMDVs) may grow by fusion to generate larger (200-300 nm) INMDVs that are ultimately released from the NE through a Dnm1-dependent or independent ONM fission step. Engagement with the phagophore occurs at or just after ONM fission. Autophagosomes containing double membrane nuclear derived vesicles (NDVs) fuse with vacuoles. Some INMDVs may also be capable of transiting through the broader ER but their fate remains uncertain.

B) A graphical representation of the three phases of Atg39 dynamics (colors) with scatter plot depicting the timing of the indicated events relative to the first detection of an Atg39-GFP focus. The approximate time of the three different phases of Atg39-GFP mobility are overlaid on the graph in red (phase 1), yellow (phase 2), and green (phase 3) Data points come from Figure 2, 3, and S3. The red line indicates the median value.

767 ## Movies

768 **Movie 1. LLSM movie of Atg39-GFP dynamics in WT cells.** A 5-minute timeseries of cells
769 expressing Atg39-GFP and Vph1-mCherry imaged every 10 seconds by LLSM. Vph1-mCherry
770 signal is rendered as a surface (magenta) and Atg39-GFP foci are rendered as balls (green).
771 Scale bar is 10 μm. Frame rate is 24 frames per second.

772 **Movie 2. CLEM and tomography of potential interface between NDV in an**
773 **autophagosome and the vacuole in a WT cell.** Electron tomogram of a cell expressing Atg39-
774 hfYFP, Nup170-mCherry, and Vph1-mCherry obtained at a site of Atg39-hfYFP accumulation
775 shown in Figure 4D. Note that the outer membrane of the autophagosome and the vacuole
776 extend towards each other but do not touch. However, content with similar electron density of
777 the vacuole lumen is observed between the inner and outer membrane of the autophagosome
778 suggesting prior fusion with the vacuole. NE, green; INMDV, blue; autophagic membranes,
779 orange; vacuole, magenta. Scale bar is 100 nm.

780 **Movie 3. CLEM and tomography of an INMDV within the NE/ER lumen engaged with a**
781 **phagophore in a *dnm1Δ* cell.** Electron tomogram of a cell expressing Atg39-hfYFP, Nup170-
782 mCherry, and Vph1-mCherry in a *dnm1Δ* cell obtained at a region of Atg39-hfYFP accumulation
783 shown in Figure 5D. NE, green; INMDV, blue; autophagic membranes, orange; vacuole,
784 magenta. Scale bar is 100 nm.

785 ## Supplementary Tables

786 **Supplementary Table 1. List of yeast strains used in this study.**

787 **Supplementary Table 2. List of plasmids used in this study.**

788 **Supplementary Table 3. List of primers used in this study.**

References

1. Mannino PJ, Lusk CP. Quality control mechanisms that protect nuclear envelope identity and function. *J Cell Biol*. Sep 5 2022;221(9)doi:10.1083/jcb.202205123
2. Mucino-Hernandez G, Acevo-Rodriguez PS, Cabrera-Benitez S, Guerrero AO, Merchant-Larios H, Castro-Obregon S. Nucleophagy contributes to genome stability through degradation of type II topoisomerases A and B and nucleolar components. *J Cell Sci*. Jan 1 2023;136(1)doi:10.1242/jcs.260563
3. Hasper J, Welle K, Swovick K, Hryhorenko J, Ghaemmaghami S, Buchwalter A. Long lifetime and tissue-specific accumulation of lamin A/C in Hutchinson-Gilford progeria syndrome. *J Cell Biol*. Jan 1 2024;223(1)doi:10.1083/jcb.202307049
4. Tsai PL, Zhao C, Turner E, Schlieker C. The Lamin B receptor is essential for cholesterol synthesis and perturbed by disease-causing mutations. *Elife*. Jun 23 2016;5doi:10.7554/eLife.16011
5. Papandreou ME, Tavernarakis N. Nucleophagy: from homeostasis to disease. *Cell Death Differ*. Mar 2019;26(4):630-639. doi:10.1038/s41418-018-0266-5
6. Natarajan N, Foresti O, Wendrich K, Stein A, Carvalho P. Quality Control of Protein Complex Assembly by a Transmembrane Recognition Factor. *Mol Cell*. Jan 2 2020;77(1):108-119 e9. doi:10.1016/j.molcel.2019.10.003
7. Khmelinskii A, Blaszczak E, Pantazopoulou M, et al. Protein quality control at the inner nuclear membrane. *Nature*. Dec 18 2014;516(7531):410-3. doi:10.1038/nature14096
8. Smoyer CJ, Smith SE, Gardner JM, McCroskey S, Unruh JR, Jaspersen SL. Distribution of Proteins at the Inner Nuclear Membrane Is Regulated by the Asi1 E3 Ligase in Saccharomyces cerevisiae. *Genetics*. Apr 2019;211(4):1269-1282. doi:10.1534/genetics.119.301911
9. Dou Z, Xu C, Donahue G, et al. Autophagy mediates degradation of nuclear lamina. *Nature*. Nov 5 2015;527(7576):105-9. doi:10.1038/nature15548
10. King GA, Goodman JS, Schick JG, et al. Meiotic cellular rejuvenation is coupled to nuclear remodeling in budding yeast. *Elife*. Aug 9 2019;8doi:10.7554/eLife.47156
11. King GA, Wettstein R, Varberg JM, et al. Meiotic nuclear pore complex remodeling provides key insights into nuclear basket organization. *J Cell Biol*. Feb 6 2023;222(2)doi:10.1083/jcb.202204039
12. Mizuno T, Irie K. Msn2/4 transcription factors positively regulate expression of Atg39 ER-phagy receptor. *Sci Rep*. Jun 7 2021;11(1):11919. doi:10.1038/s41598-021-91480-0
13. Papandreou ME, Konstantinidis G, Tavernarakis N. Nucleophagy delays aging and preserves germline immortality. *Nat Aging*. Jan 2023;3(1):34-46. doi:10.1038/s43587-022-00327-4
14. Bahmanyar S, Biggs R, Schuh AL, et al. Spatial control of phospholipid flux restricts endoplasmic reticulum sheet formation to allow nuclear envelope breakdown. *Genes Dev*. Jan 15 2014;28(2):121-6. doi:10.1101/gad.230599.113
15. Campbell JL, Lorenz A, Witkin KL, Hays T, Loidl J, Cohen-Fix O. Yeast nuclear envelope subdomains with distinct abilities to resist membrane expansion. *Mol Biol Cell*. Apr 2006;17(4):1768-78. doi:10.1091/mbc.e05-09-0839

16. Romanauska A, Kohler A. Lipid saturation controls nuclear envelope function. *Nat Cell Biol*. Sep 2023;25(9):1290-1302. doi:10.1038/s41556-023-01207-8
17. Santos-Rosa H, Leung J, Grimsey N, Peak-Chew S, Siniossoglou S. The yeast lipin Smp2 couples phospholipid biosynthesis to nuclear membrane growth. *EMBO J*. 2005;24
18. Barbosa AD, Lim K, Mari M, et al. Compartmentalized Synthesis of Triacylglycerol at the Inner Nuclear Membrane Regulates Nuclear Organization. *Dev Cell*. Sep 23 2019;50(6):755-766 e6. doi:10.1016/j.devcel.2019.07.009
19. Romanauska A, Kohler A. The Inner Nuclear Membrane Is a Metabolically Active Territory that Generates Nuclear Lipid Droplets. *Cell*. Jul 26 2018;174(3):700-715 e18. doi:10.1016/j.cell.2018.05.047
20. Romanauska A, Kohler A. Reprogrammed lipid metabolism protects inner nuclear membrane against unsaturated fat. *Dev Cell*. Sep 27 2021;56(18):2562-2578 e3. doi:10.1016/j.devcel.2021.07.018
21. Melia TJ, Lystad AH, Simonsen A. Autophagosome biogenesis: From membrane growth to closure. *J Cell Biol*. Jun 1 2020;219(6)doi:10.1083/jcb.202002085
22. Kucinska MK, Fedry J, Galli C, et al. TMX4-driven LINC complex disassembly and asymmetric autophagy of the nuclear envelope upon acute ER stress. *Nat Commun*. Jun 13 2023;14(1):3497. doi:10.1038/s41467-023-39172-3
23. Roberts P, Moshitch-Moshkovitz S, Kvam E, O'Toole E, Winey M, Goldfarb DS. Piecemeal microautophagy of nucleus in Saccharomyces cerevisiae. *Mol Biol Cell*. Jan 2003;14(1):129-41. doi:10.1091/mbc.e02-08-0483
24. Allegretti M, Zimmerli CE, Rantos V, et al. In-cell architecture of the nuclear pore and snapshots of its turnover. *Nature*. Oct 2020;586(7831):796-800. doi:10.1038/s41586-020-2670-5
25. Lee CW, Wilfling F, Ronchi P, et al. Selective autophagy degrades nuclear pore complexes. *Nat Cell Biol*. Feb 2020;22(2):159-166. doi:10.1038/s41556-019-0459-2
26. Tomioka Y, Kotani T, Kirisako H, et al. TORC1 inactivation stimulates autophagy of nucleoporin and nuclear pore complexes. *J Cell Biol*. Jul 6 2020;219(7)doi:10.1083/jcb.201910063
27. Mochida K, Oikawa Y, Kimura Y, et al. Receptor-mediated selective autophagy degrades the endoplasmic reticulum and the nucleus. *Nature*. Jun 18 2015;522(7556):359-62. doi:10.1038/nature14506
28. Mizuno T, Muroi K, Irie K. Snf1 AMPK positively regulates ER-phagy via expression control of Atg39 autophagy receptor in yeast ER stress response. *PLoS Genet*. Sep 2020;16(9):e1009053. doi:10.1371/journal.pgen.1009053
29. Otto FB, Thumm M. Mechanistic dissection of macro- and micronucleophagy. *Autophagy*. Mar 2021;17(3):626-639. doi:10.1080/15548627.2020.1725402
30. Chandra S, Mannino PJ, Thaller DJ, et al. Atg39 selectively captures inner nuclear membrane into lumenal vesicles for delivery to the autophagosome. *J Cell Biol*. Dec 6 2021;220(12)doi:10.1083/jcb.202103030
31. Mochida K, Otani T, Katsumata Y, et al. Atg39 links and deforms the outer and inner nuclear membranes in selective autophagy of the nucleus. *J Cell Biol*. Feb 7 2022;221(2)doi:10.1083/jcb.202103178
32. Otsuga D, Keegan BR, Brisch E, et al. The Dynamin-related GTPase, Dnm1p, Controls Mitochondrial Morphology in Yeast. *J Cell Biol*. 1998;143(2)

879 33. Kuravi K, Nagotu S, Krikken AM, et al. Dynamin-related proteins Vps1p and
880 Dnm1p control peroxisome abundance in Saccharomyces cerevisiae. *J Cell Sci*. Oct 1
881 2006;119(Pt 19):3994-4001. doi:10.1242/jcs.03166
882 34. Gonzalez A, Covarrubias-Pinto A, Bhaskara RM, et al. Ubiquitination regulates
883 ER-phagy and remodelling of endoplasmic reticulum. *Nature*. Jun 2023;618(7964):394-
884 401. doi:10.1038/s41586-023-06089-2
885 35. Rosado CJ, Mijaljica D, Hatzinisiriou I, Prescott M, Devenish RJ. Rosella: a
886 fluorescent pH-biosensor for reporting vacuolar turnover of cytosol and organelles in
887 yeast. *Autophagy*. Feb 2008;4(2):205-13. doi:10.4161/auto.5331
888 36. Kim J, Kamada Y, Stromhaug PE, et al. Cvt9/Gsa9 Functions in Sequestering
889 Selective Cytosolic Cargo Destined for the Vacuole. *Journal of Cell Biology*.
890 2001;153(1)
891 37. Kirisako T, Baba M, Ishihara N, et al. Formation Process of Autophogosome is
892 Traced with Apg8/Aut7p in Yeast. *Journal of Cell Biology*. 1999;147(2)
893 38. Kvam E, Goldfarb DS. Nvj1p is the outer-nuclear-membrane receptor for
894 oxysterol-binding protein homolog Osh1p in Saccharomyces cerevisiae. *J Cell Sci*. Oct
895 1 2004;117(Pt 21):4959-68. doi:10.1242/jcs.01372
896 39. Borah S, Thaller DJ, Hakhverdyan Z, et al. Heh2/Man1 may be an evolutionarily
897 conserved sensor of NPC assembly state. *Mol Biol Cell*. Jul 15 2021;32(15):1359-1373.
898 doi:10.1091/mbc.E20-09-0584
899 40. Thaller DJ, Allegretti M, Borah S, Ronchi P, Beck M, Lusk CP. An ESCRT-LEM
900 protein surveillance system is poised to directly monitor the nuclear envelope and
901 nuclear transport system. *Elife*. Apr 3 2019;8doi:10.7554/eLife.45284
902 41. Webster BM, Colombi P, Jager J, Lusk CP. Surveillance of nuclear pore complex
903 assembly by ESCRT-III/Vps4. *Cell*. Oct 9 2014;159(2):388-401.
904 doi:10.1016/j.cell.2014.09.012
905 42. Webster BM, Thaller DJ, Jager J, Ochmann SE, Borah S, Lusk CP. Chm7 and
906 Heh1 collaborate to link nuclear pore complex quality control with nuclear envelope
907 sealing. *EMBO J*. 2016;35
908 43. Chen S, Cui Y, Parashar S, Novick PJ, Ferro-Novick S. ER-phagy requires Lnp1,
909 a protein that stabilizes rearrangements of the ER network. *Proc Natl Acad Sci U S A*.
910 Jul 3 2018;115(27):E6237-E6244. doi:10.1073/pnas.1805032115
911 44. Chen S, Mari M, Parashar S, et al. Vps13 is required for the packaging of the ER
912 into autophagosomes during ER-phagy. *Proc Natl Acad Sci U S A*. Aug 4
913 2020;117(31):18530-18539. doi:10.1073/pnas.2008923117
914 45. Cui Y, Parashar S, Zahoor M, et al. A COPII subunit acts with an autophagy
915 receptor to target endoplasmic reticulum for degradation. *Science*. Jul 5
916 2019;365(6448):53-60. doi:10.1126/science.aau9263
917 46. Liu D, Mari M, Li X, Reggiori F, Ferro-Novick S, Novick P. ER-phagy requires the
918 assembly of actin at sites of contact between the cortical ER and endocytic pits. *Proc
919 Natl Acad Sci U S A*. Feb 8 2022;119(6)doi:10.1073/pnas.2117554119
920 47. Anwar K, Klemm RW, Condon A, et al. The dynamin-like GTPase Sey1p
921 mediates homotypic ER fusion in S. cerevisiae. *J Cell Biol*. Apr 16 2012;197(2):209-17.
922 doi:10.1083/jcb.201111115

48. Voeltz GK, Prinz WA, Shibata Y, Rist JM, Rapoport TA. A class of membrane proteins shaping the tubular endoplasmic reticulum. *Cell*. Feb 10 2006;124(3):573-86. doi:10.1016/j.cell.2005.11.047
49. Mozdy AD, McCaffery JM, Shaw JM. Dnm1p GTPase-mediated Mitochondrial Fission Is a Multi-step Process Requiring the Novel Integral Membrane Component Fis1p. *J Cell Biol*. 2000;151
50. Sesaki H, Southard SM, Yaffe MP, Jensen RE. Mgm1p, a dynamin-related GTPase, is essential for fusion of the mitochondrial outer membrane. *Mol Biol Cell*. Jun 2003;14(6):2342-56. doi:10.1091/mbc.e02-12-0788
51. Smaczynska-de R, II, Allwood EG, Aghamohammadzadeh S, Hettema EH, Goldberg MW, Ayscough KR. A role for the dynamin-like protein Vps1 during endocytosis in yeast. *J Cell Sci*. Oct 15 2010;123(Pt 20):3496-506. doi:10.1242/jcs.070508
52. Ferguson SM, De Camilli P. Dynamin, a membrane-remodelling GTPase. *Nat Rev Mol Cell Biol*. Jan 11 2012;13(2):75-88. doi:10.1038/nrm3266
53. Motley AM, Ward GP, Hettema EH. Dnm1p-dependent peroxisome fission requires Caf4p, Mdv1p and Fis1p. *J Cell Sci*. May 15 2008;121(Pt 10):1633-40. doi:10.1242/jcs.026344
54. Naylor K, Ingerman E, Okreglak V, Marino M, Hinshaw JE, Nunnari J. Mdv1 Interacts with Assembled Dnm1 to Promote Mitochondrial Division. *Journal of Biological Chemistry*. 2006;281(4):2177-2183. doi:10.1074/jbc.M507943200
55. Mao K, Wang K, Liu X, Klionsky DJ. The scaffold protein Atg11 recruits fission machinery to drive selective mitochondria degradation by autophagy. *Dev Cell*. Jul 15 2013;26(1):9-18. doi:10.1016/j.devcel.2013.05.024
56. Mao K, Liu X, Feng Y, Klionsky DJ. The progression of peroxisomal degradation through autophagy requires peroxisomal division. *Autophagy*. Apr 2014;10(4):652-61. doi:10.4161/auto.27852
57. Ader NR, Chen L, Surovtsev IV, et al. An ESCRT grommet cooperates with a diffusion barrier to maintain nuclear integrity. *Nat Cell Biol*. Oct 2023;25(10):1465-1477. doi:10.1038/s41556-023-01235-4
58. Bailey MLP, Surovtsev I, Williams JF, et al. Loops and the activity of loop extrusion factors constrain chromatin dynamics. *Mol Biol Cell*. Jul 1 2023;34(8):ar78. doi:10.1091/mbc.E23-04-0119
59. Crocker JC, Grier DG. Methods of digital video microscopy for colloidal studies. *Journal of colloid and interface science*. 1996;179
60. Lawrimore J, Bloom KS, Salmon ED. Point centromeres contain more than a single centromere-specific Cse4 (CENP-A) nucleosome. *J Cell Biol*. Nov 14 2011;195(4):573-82. doi:10.1083/jcb.201106036
61. Campbell BC, Paez-Segala MG, Looger LL, Petsko GA, Liu CF. Chemically stable fluorescent proteins for advanced microscopy. *Nat Methods*. Dec 2022;19(12):1612-1621. doi:10.1038/s41592-022-01660-7
62. Bieber A, Capitanio C, Erdmann PS, et al. In situ structural analysis reveals membrane shape transitions during autophagosome formation. *Proc Natl Acad Sci U S A*. Sep 27 2022;119(39):e2209823119. doi:10.1073/pnas.2209823119

63. Hollenstein DM, Licheva M, Konradi N, et al. Spatial control of avidity regulates initiation and progression of selective autophagy. *Nat Commun*. Dec 10 2021;12(1):7194. doi:10.1038/s41467-021-27420-3
64. Villinger C, Neusser G, Kranz C, Walther P, Mertens T. 3D Analysis of HCMV Induced-Nuclear Membrane Structures by FIB/SEM Tomography: Insight into an Unprecedented Membrane Morphology. *Viruses*. Nov 4 2015;7(11):5686-704. doi:10.3390/v7112900
65. Speese SD, Ashley J, Jokhi V, et al. Nuclear envelope budding enables large ribonucleoprotein particle export during synaptic Wnt signaling. *Cell*. May 11 2012;149(4):832-46. doi:10.1016/j.cell.2012.03.032
66. Keuenhof KS, Kohler V, Broeskamp F, et al. Nuclear envelope budding and its cellular functions. *Nucleus*. Dec 2023;14(1):2178184. doi:10.1080/19491034.2023.2178184
67. Schneider BL, Seufert W, Steiner B, Yang QH, Futcher AB. Use of polymerase chain reaction epitope tagging for protein tagging in Saccharomyces cerevisiae. *Yeast*. Oct 1995;11(13):1265-74. doi:10.1002/yea.320111306
68. Longtine MS, McKenzie Iii A, Demarini DJ, et al. Additional modules for versatile and economical PCR-based gene deletion and modification in Saccharomyces cerevisiae. *Yeast*. 1998;14(10):953-961. doi:10.1002/(sici)1097-0061(199807)14:10<953::Aid-yea293>3.0.Co;2-u
69. Zhang Y, Serratore ND, Briggs SD. N-ICE plasmids for generating N-terminal 3 x FLAG tagged genes that allow inducible, constitutive or endogenous expression in Saccharomyces cerevisiae. *Yeast*. May 2017;34(5):223-235. doi:10.1002/yea.3226
70. Baudin A, Ozier-Kalogeropoulos OD, A., Lacroute F, Cullin C. A simple and efficient method for direct gene deletion in *Saccharomyces cerevisiae*. *Nucleic Acids Research*. 1993;21
71. Guldener U, Heck S, Fiedler T, Beinhauer J, Hegemann JH. A new efficient gene disruption cassette for repeated use in budding yeast. *Nucleic Acids Research*. 1996;24(13)
72. Lacy MM, Baddeley D, Berro J. Single-molecule imaging of the BAR-domain protein Pil1p reveals filament-end dynamics. *Mol Biol Cell*. Aug 15 2017;28(17):2251-2259. doi:10.1091/mbc.E17-04-0238
73. Smoyer CJ, Katta SS, Gardner JM, et al. Analysis of membrane proteins localizing to the inner nuclear envelope in living cells. *J Cell Biol*. Nov 21 2016;215(4):575-590. doi:10.1083/jcb.201607043
74. Chen BC, Legant WR, Wang K, et al. Lattice light-sheet microscopy: imaging molecules to embryos at high spatiotemporal resolution. *Science*. Oct 24 2014;346(6208):1257998. doi:10.1126/science.1257998
75. Adell MAY, Migliano SM, Upadhyayula S, et al. Recruitment dynamics of ESCRT-III and Vps4 to endosomes and implications for reverse membrane budding. *Elife*. Oct 11 2017;6doi:10.7554/eLife.31652
76. Kukulski W, Schorb M, Welsch S, Picco A, Kaksonen M, Briggs JA. Precise, correlated fluorescence microscopy and electron tomography of lowicryl sections using fluorescent fiducial markers. *Methods Cell Biol*. 2012;111:235-57. doi:10.1016/B978-0-12-416026-2.00013-3

1012 77. Mastronarde DN. Automated electron microscope tomography using robust
1013 prediction of specimen movements. *J Struct Biol*. Oct 2005;152(1):36-51.
1014 doi:10.1016/j.jsb.2005.07.007
1015 78. Kremer JRM, D. N.McIntosh J. R. Computer Visualization of Three-Dimensional
1016 Image Data Using IMOD. *Journal of Structural Biology*. 1996;116(1)
1017 79. Mastronarde DN, Held SR. Automated tilt series alignment and tomographic
1018 reconstruction in IMOD. *J Struct Biol*. Feb 2017;197(2):102-113.
1019 doi:10.1016/j.jsb.2016.07.011
1020 80. Flajolet P, Gardy D, Thimonier L. Birthday paradox, coupon collectors, caching
1021 algorithms and self-organizing search. *Discrete Applied Mathematics*. 1992;39:207-229.
1022 81. Schindelin J, Arganda-Carreras I, Frise E, et al. Fiji: an open-source platform for
1023 biological-image analysis. *Nat Methods*. Jun 28 2012;9(7):676-82.
1024 doi:10.1038/nmeth.2019

1025

1026

Supplementary Table 1: *S. cerevisiae* strains			
Name	***Genotype***	***Origin***	***Generation***
W303a	*MATa, ade2-1 can1-100 his3-11,15 leu2-3,112 trp1-1 ura3-1*	EUROSCARF	
W303α	*MATα, ade2-1 can1-100 his3-11,15 leu2-3,112 trp1-1 ura3-1*	EUROSCARF	
FIGURE 1			
PMCPL1045	W303, *Atg39-pHluorin-mCherry*	This study	Transformation of W303A with PCR product
PMCPL1078	W303, *Atg39-pHluorin-mCherry atg8Δ::natMX6*	This study	Progeny from cross between PMCPL1045 and PMCPL472
PMCPL1079	W303, *ATG39-pHluorin-mCherry atg11Δ::hphMX6*	This study	Progeny from cross between PMCPL1045 and PMCPL472
PMCPL1253	W303, *ATG39-pHluorin-mCherry nvj1Δ::hphMX6*	This study	Progeny from cross between PMCPL1067 and BWCPL1088
PMCPL1130	W303, *ATG39-pHluorin-mCherry vps13Δ::kanMX6*	This study	Progeny from cross between PMCPL1069 and DTCPL1702
PMCPL1282	W303, *ATG39-pHluorin-mCherry lst1Δ::kanMX6*	This study	Progeny from cross between PMCPL1078 and PMCPL1260
PMCPL1066	W303, *ATG39-pHluorin-mCherry scs2Δ::kanMX6*	This study	Transformation of PMCPL1045 with PCR product
PMCPL1249	W303, *ATG39-pHluorin-mCherry lnp1Δ::hphMX6*	This study	Progeny from cross between PMCPL1078 and DTCPL1448
PMCPL1276	W303, *ATG39-pHluorin-mCherry sey1Δ::kanMX6*	This study	Progeny from cross between PMCPL1256 and PMCPL300
PMCPL1243	W303, *ATG39-pHluorin-mCherry rtn1Δ::his3MX6 rtn2Δ::TRP1 yop1Δ::hphMX6*	This study	Progeny from cross between PMCPL1066 and BWCPL176
PMCPL1252	W303, *ATG39-pHluorin-mCherry vps1Δ::his3MX6*	This study	Progeny from cross between PMCPL1067 and PMCPL1094
PMCPL1264	W303, *ATG39-pHluorin-mCherry mgm1Δ::hphMX6*	This study	Progeny from cross between PMCPL1045 and PMCPL1251
PMCPL1067	W303, *ATG39-pHluorin-mCherry dnm1Δ::kanMX6*	This study	Progeny from cross between PMCPL1045 and PMCPL928
PMCPL1127	W303, *ATG39-pHluorin-mCherry heh1Δ::hphMX6*	This study	Progeny from cross between PMCPL1067 and BWCPL1476
PMCPL1293	W303, *ATG39-pHluorin-mCherry heh2Δ::kanMX6*	This study	Progeny from cross between PMCPL1124 and CPL1222
PMCPL1124	W303, *ATG39-pHluorin-mCherry chm7Δ::hphMX6*	This study	Progeny from cross between PMCPL1067 and BWCPL1632
FIGURE 2			
PMCPL1319	W303, *ATG39-mEGFP DNM1-mCherry::natMX6 pRS406-DNM1 fis1Δ::hphMX6*	This study	Transformation of PCR product into PMCPL840
PMCPL1087	W303, *ATG39-mEGFP DNM1-mCherry::natMX6 pRS406-dnm1(K41A) fis1Δ::hphMX6*	This study	Transformation of PCR product into PMCPL832
FIGURE 3			
PMCPL940	W303, *ATG39-mEGFP VPH1-3xHA-mCherry::natMX6*	This study	Progeny from cross between PMCPL856 and PMCPL922
PMCPL857	W303, *ATG39-mEGFP VPH1-3xHA-mCherry::natMX6 NUP170-mCherry::kanMX6 dnm1Δ::TRP1*	This study	Progeny from cross between PMCPL851 and PMCPL608
MKSP3186	*fta3::fta3-mEGFP::kanMX6 leu1-32 ura3-D18 ade6-M210*	Ader et al., 2023	
FIGURE 4			
PMCPL1283	W303, *ATG39-hfYFP VPH1-3xHA-mCherry::natMX6 NUP170-mCherry::kanMX6*	This study	Progeny from cross between PMCPL1257 and PMCPL850
PMCPL1390	W303, *ATG39-hfYFP VPH1-3xHA-mCherry::natMX6 NUP170-mCherry::kanMX6 dnm1Δ::TRP1*	This study	Progeny from cross between PMCPL1283 and PMCPL785
FIGURE 5			
PMCPL1390	W303, *ATG39-hfYFP VPH1-3xHA-mCherry::natMX6 NUP170-mCherry::kanMX6 dnm1Δ::TRP1*	This study	Progeny from cross between PMCPL1283 and PMCPL785
FIGURE S1			
PMCPL1263	W303, *ATG39-3xHA::his3MX6*	This study	Progeny from cross between PMCPL300 and SCCPL117
PMCPL578	W303, *ATG39-3xHA*	This study	Transformation of PCR product into W303A
PMCPL521	W303, *ATG39-mEGFP::kanMX6*	This study	Transformation of PCR product into W303A
PMCPL1193	W303, *ATG39-mEGFP*	This study	Transformation of PCR product into W303A
FIGURE S2			
PMCPL1319	W303, *ATG39-mEGFP DNM1-mCherry::natMX6 pRS406-DNM1 fis1Δ::hphMX6*	This study	Transformation of PCR product into PMCPL840
PMCPL1087	W303, *ATG39-mEGFP DNM1-mCherry::natMX6 pRS406-dnm1(K41A) fis1Δ::hphMX6*	This study	Transformation of PCR product into PMCPL832
PMCPL1112	W303, *ATG39-phluorin DNM1-mCherry::natMX6 pRS406-dnm1(K41A) fis1Δ::hphMX6*	This study	Transformation of PCR product into PMCPL1110
PMCPL1113	W303, *ATG39-phluorin DNM1-mCherry::natMX6 pRS406-dnm1(K41A) fis1Δ::kanMX6 atg11Δ::hphM*	This study	Transformation of PCR product into PMCPL1111
FIGURE S3			
PMCPL940	W303, *ATG39-mEGFP VPH1-3xHA-mCherry::natMX6*	This study	Progeny from cross between PMCPL856 and PMCPL922
PMCPL857	W303, *ATG39-mEGFP VPH1-3xHA-mCherry::natMX6 NUP170-mCherry::kanMX6 dnm1Δ::TRP1*	This study	Progeny from cross between PMCPL851 and PMCPL608
PMCPL1132	W303, *ATG39-mEGFP pRS405-heh1-1-476-2xmCherry*	This study	Transformation of linearized plasmid into PMCPL1120
FIGURE S4			
PMCPL1283	W303, *ATG39-hfYFP VPH1-3xHA-mCherry::natMX6 NUP170-mCherry::kanMX6*	This study	Progeny from cross between PMCPL1257 and PMCPL850
FIGURE S5			
PMCPL1390	W303, *ATG39-hfYFP VPH1-3xHA-mCherry::natMX6 NUP170-mCherry::kanMX6 dnm1Δ::TRP1*	This study	Progeny from cross between PMCPL1283 and PMCPL785

Table S2: Plasmids used in this study

Name	*Description*	*Origin*
pFa6a-mEGFP-kanMX6	Template for PCR based chromosomal integration of mEGFP ORF	Lacy et al. 2017
pFA6a-hphMX6	Template for PCR based chromosomal integration of hphMX6 cassette	Longtine et al. 1998
pFA6a-natMX6	Template for PCR based chromosomal integration of natMX6 cassette	Van Driessche et al. 2005
pFA6a-kanMX6	Template for PCR based chromosomal integration of kanMX6 cassette	Bahler J. et al. 1998
pAS1NB	Template for cloning pPM27	Rosado et al. 2008
pSJ1321	Template for cloning pPM30	Smoyer et al. 2016
pFA6a-3xHA-mCherry-natMX6	Template for PCR based chromosomal integration of 3xHA-mCherry ORF	This study
pFA6a-3xHA-his3MX6	Template for PCR based chromosomal integration of 3xHA	Longtine et al. 1998
pPM09	mEGFP-loxP-kanMX6-loxP	This study
pPM26	3xHA-loxP-kanMX6-loxP	This study
pPM31	hfYFP-loxP-kanMX6-loxP	This study
pPM27	pHlourin-loxP-kanMX6-loxP	This study
pPM28	pHlourin-mCherry-loxP-kanMX6-loxP	This study
pFA6a-mCherry-kanMX6	Template for PCR based chromosomal integration of mCherry ORF	This study
pPM03	pRS406 ATG8pr	This study
pPM11	pRS406 ATG8pr-*DNM1*	This study
pPM15	pRS406 *dnm1 (K41A)*	This study
pSH47	pRS416 *GAL1-CRE*	Güldener et al. 1996
pPM29	pRS405 heh1-1-479-mCherry	This study
pPM30	pRS405 heh1-1-479-2xmCherry	This study
pPM32	mCherry-loxP-kanMX6-loxP	This study

1029

1030

Table S3: Primers used in this study		
Purpose	***Name***	***Sequence***
Atg39 C-terminal tag cassette construction	F2 ATG39	TCGAGGATGTATAAAGCGATGTCAGAATGCAGGAAAAAAAATTATTTTAAGTGCAAACAC-CGGATCCCCGGGTTAATTAA
	R1 ATG39	TAAGCAGTCGTTTTTTTTTTCTTTTGTTAATTTCATTCTTCATGCTGGGTTTTGGATGAT-GAATTCGAGCTCGTTTAAAC
	P1.4 ATG39	TAAGCAGTCGTTTTTTTTTTCTTTTGTTAATTTCATTCTTCATGCTGGGTTTTGGATGAT-atggtgtcgacaacccttaat
	F5 GFP ATG39	TCGAGGATGTATAAAGCGATGTCAGAATGCAGGAAAAAAAATTATTTTAAGTGCAAACAC-AAAGGAGAAGAACTTTTCACTGG
	F5 HA ATG39	TCGAGGATGTATAAAGCGATGTCAGAATGCAGGAAAAAAAATTATTTTAAGTGCAAACAC-gccactagtTACCCATACGAT
	F5 hfYFP ATG39	TCGAGGATGTATAAAGCGATGTCAGAATGCAGGAAAAAAAATTATTTTAAGTGCAAACAC-GTATCCAAGGGTGAGGAATTG
Vph1 C-terminal tag cassette construction	F2 VPH1	GCATTTGAGTATAAAGACATGGAAGTCGCTGTTGCTAGTGCAAGCTCTTCCGCTTCAAGC-CGGATCCCCGGGTTAATTAA
	R1 VPH1	ATGGTCACTGGTGGATTGGATTGCAAGTCTAACGTTTTCATGAGATAAGTTTGGCTTTCC-GAATTCGAGCTCGTTTAAAC
Nup170 C-terminal tag cassette construction	F2 NUP170	CCAATTGAAAAGTACGTTAAGAACAGCGGCAATAATTTGGGGATTTGTTTCTACAAAGAA-CGGATCCCCGGGTTAATTAA
	R1 NUP170	ACCTTTATCTTAAGGAAAAGTTCACTCGATATTCTTAACTTTACCGTCTAGTAAGGCCTC-GAATTCGAGCTCGTTTAAAC
scs2Δ cassette construction	F1 SCS2	CGCACATTCTGTGTTAATAGTGTAGCAGAAGGGTATTCTACAATCTCCGCGAACCTAAGT-CGGATCCCCGGGTTAATTAA
	R1 SCS2	GGAAAGGGCAAAACACACACATATATAAATATATATTTAGAATACAGCTATATCCTCAATCTCCC-GAATTCGAGCTCGTTTAAAC
fis1Δ cassette construction	F1 FIS1	ATACCTTGCGTAAAAACGGCACATAGAAGCACAGATCAGAGCACAGCCATACAACATAAG-CGGATCCCCGGGTTAATTAA
	R1 FIS1	TACGCGTGCGTGCGATTCATTCTTATGTATGTACGTATGTGCTGATTTTTTATGTGCTTG-GAATTCGAGCTCGTTTAAAC
RTqPCR primers	sATG39 qPCR 6	TGAAAGACGGTTGGCACAAG
	asATG39 qPCR 6	ACCCTTAAACTTTCTTGAGCGG
	sATG8 qPCR	GAAGGCCATCTTCATTTTTGTC
	asATG8 qPCR	TTCTCCTGAGTAAGTGACATAC
	sATG11 qPCR	GCAGACGTAGATCTTTCGCG
	asATG11 qPCR	TGTGAGCAAACGGTTAAGCC
	sATG40 qPCR	GAGACCCTTTGTAACGGAGC
	asATG40 qPCR	CATTCGGGAACTCAGTGCTG
	sACT1 qPCR	TGGATTCCGGTGATGGTGTT
	asACT1 qPCR	TCAAAATGGCGTGAGGTAGAG

1031